Industrial Chemistry & Materials

ROYAL SOCIETY OF CHEMISTRY

REVIEW

View Article Online
View Journal | View Issue

Cite this: *Ind. Chem. Mater.*, 2024, **2**, 57

Recent advances in the synthesis, characterization, and catalytic consequence of metal species confined within zeolite for hydrogen-related reactions

Meng Liu, Caixia Miao and Zhijie Wu *

Zeolites-encapsulated metal and metal oxide species are important heterogeneous catalysts. They give performances that steadily outperform traditional supported catalysts in many important reactions and have become a research hotspot. Remarkable achievements have been made with respect to the synthesis, characterization, and performances of metal species (typically metal and metal oxide clusters) confined in zeolites. The development in the strategies for the encapsulation of metal species including post-treatment and *in situ* synthesis method are introduced and compared. For the characterization of zeolite-encapsulated metal catalysts, the structural and surface properties of metal species are studied by several useful techniques, such as electron microscopy, X-ray absorption (XAS), Fourier transform infrared spectroscopy of CO (FTIR-CO), and chemisorption, which confirm the successful confinement of metal species in zeolites and their unique physiochemical properties. In addition, the encapsulation fraction can be determined by a probe molecular titration reaction. For the catalytic performance of zeolite-encapsulated metal catalysts, the activity, selectivity, and stability are emphasized. Finally, applications of zeolite-encapsulated metal catalysts in hydrogen-related reactions are summarized.

Received 6th July 2023,
Accepted 25th August 2023

DOI: 10.1039/d3im00074e

rsc.li/icm

Keywords: Zeolite; Encapsulation; Metal species; Synthesis; Characterization; Catalytic performance.

State Key Laboratory of Heavy Oil Processing and the Key Laboratory of Catalysis of CNPC, China University of Petroleum-Beijing, Beijing 102249, China.
E-mail: zhijiewu@cup.edu.cn

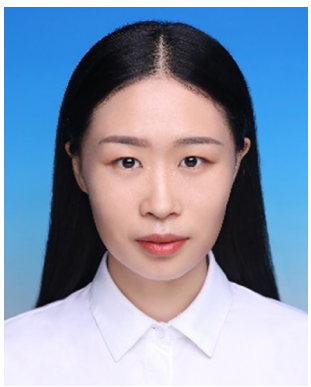

Meng Liu

Meng Liu received her Master's degree from China University of Petroleum-Beijing in 2021. Now she is a Ph.D. student at the China University of Petroleum-Beijing. Her research interest focuses on the controlled synthesis and catalytic applications of zeolites.

Zhijie Wu

Zhijie Wu received his B.S. degree in Chemistry from Nankai University in June 2004 and his Ph.D. degree in Physical Chemistry from Nankai University in June 2009. After obtaining his PhD, he worked as a postdoctoral fellow at the Department of Chemical and Biomolecular Engineering, University of California at Berkeley (2009–2011). Thereafter, he joined as a lecturer at China University of Petroleum-Beijing. Now, he is the full professor of the State Key Laboratory of Heavy Oil Processing and the Department of Energy and Catalysis Engineering, College of Chemical Engineering and Environment. His current interests of research relate to the synthesis and the structural and mechanistic characterization of catalytic materials and catalyst for chemical reactions important in energy conversion and petrochemical engineering.

1 Introduction

Metal catalysts are an important class of catalytic materials, which have been widely used in various chemical reactions such as redox, hydrogenation, and coupling reactions in the past few decades.[1–3] It has been extensively reported in the literature that the small metal particle size contributes to the greater exposure of active sites as well as higher reactivity.[4,5] However, small metal particles generally have low thermal stability and tend to sinter, coalesce, or leach under harsh reaction conditions, even when they have strong interaction with supports.[6–8] Therefore, deactivation due to sintering and leaching during the reaction process is one of the most important problems for the practical application of metal catalysts with small metal particle size. Currently, confining metal species within graphene oxide,[9–11] nanoporous carbon,[12] metal–organic frameworks,[13,14] and zeolites[15–17] is a promising method to solve this problem. Specially, zeolite-encapsulated metal catalysts have earned increasing attention due to their unique catalytic activity, selectivity, and stability from the confinement effect.

Indeed, zeolites are one of the ideal substrates for encapsulation. First, zeolites are kind of crystalline aluminosilicate with rigid matrix that provide high specific surface area and high thermal and hydrothermal stability.[18,19] Encapsulating metal species into zeolite micropores, channels, cages, or cavities can stabilize metal species by suppressing their movement and growth through spatial constraints.[15,20] In some case, spatial constraints can prevent these metal species from the accessing toxic substances in the reaction medium, thereby reducing their deactivation. Second, the well-defined microporous structure of the zeolite can select reactants, transition states, and products according to the molecular size,[21,22] and "shape-selective catalysis" can be realized over encapsulated metal catalysts. Third, the synchronization of acid sites and metal sites makes bifunctional catalysts applicable for tandem catalytic reactions with excellent activity and surprising selectivity.[23–27]

This review starts from the encapsulation strategies of metal species confined in zeolites, and the recent progresses are demonstrated. We firstly introduce the recent achievements of the synthesis approaches and discuss the recent methods for the characterization of zeolite-encapsulated metal catalysts. Then, the performance of zeolite-encapsulated metal catalysts in terms of activity, selectivity, stability, and applications in hydrogen-related reactions are described.

2 Classification of metal species confined in zeolites

The incorporation of metal species into zeolite generally results in two kinds of modified zeolite materials, the substitution of framework Al or Si atom by metal cations to form heteroatomic zeolite and the confinement of metal species within zeolite micropores, channels, cages, or cavities (denoted as metal@zeolite), in which the metal species would be stabilized and distributed by the confinement environment *via* the strong interaction between metal species and zeolite framework. Here, we regard the strategy for the metal@zeolite materials as metal encapsulation. As shown in Fig. 1, based on the origin of metal species within zeolites, three types of zeolite-encapsulated metal catalysts can be assigned. First, metal atoms embedded within zeolite framework are removed and transferred into zeolite channels or pores *via* calcination or reduction process.[28,29] Kurbanova *et al.*[30] obtained Fe@MFI (Al-free MFI zeolite encapsulated Fe metal) by the reduction of Fe-MFI (Fe atom sitting in MFI zeolite framework) in a flow of H_2/N_2 mixture at 900 °C for 10 h. Second, metal species without capability of incorporating into the zeolite framework (*e.g.* Pt, Pd or Ni) are introduced within zeolite micropores and then calcinated or reduced to encapsulated metal or metal oxides, such as Ni@NaX,[31] Pd@SOD,[32] Pt@S-1,[33] and Fe_3O_4@ZSM-5.[34] These metal clusters with 1–2 nm are encapsulated within zeolite micropores or channels and restricted by small zeolite aperture (<0.7 nm) and show excellent thermal stability and resistance to large poisoning reactants.[35–37] Nevertheless, the accessibility of these encapsulated metal clusters to reactants is somewhat prevented due to the diffusion barrier throughout the zeolite aperture. Therefore, hierarchical zeolites with mesopore pores are developed to confine metal species,[38–41] and the metal particles within the intracrystalline mesopore of zeolites are the third type of encapsulated metal species.

3 Encapsulation strategy

Two typical synthesis strategies for zeolite encapsulation, including post-treatment (*i.e.*, ion-exchanging, interzeolite transformation, and recrystallization) and *in situ* synthesis (*i.e.*, *in situ* hydrothermal and dry-gel synthesis), have been developed. Specifically, the *in situ* hydrothermal synthesis and dry-gel conversion are frequently developed. The synthesis of some selected encapsulated metal catalysts and their applications are presented in Table 1. Clearly, these zeolite-encapsulated metal samples are characteristic of excellent activity and selectivity in the catalytic reaction.

3.1 Post-treatment

Zeolite-encapsulated metal species can be achieved by one-step post-treatment and multistep post-treatment, respectively. The commonly reported impregnation, ion-exchanging, and deposition–precipitation approaches are ascribed to one-step post-treatment strategy to directly deposit metal species.[51–53] The multistep post-treatment method generally includes dealumination[54] or desilication,[55] recrystallization,[47] interzeolite transformation,[56,57] and combined introduction of metal species, respectively.

3.1.1 One-step post-treatment. Impregnation is the most reported method to prepare zeolite-supported metal catalysts but leads to a random distribution of metal species. Specially, large metal hydrated ions cannot penetrate the zeolite aperture and then aggregate at the external surface,[58,59] resulting in large metal particles after subsequent calcination and reduction treatment.

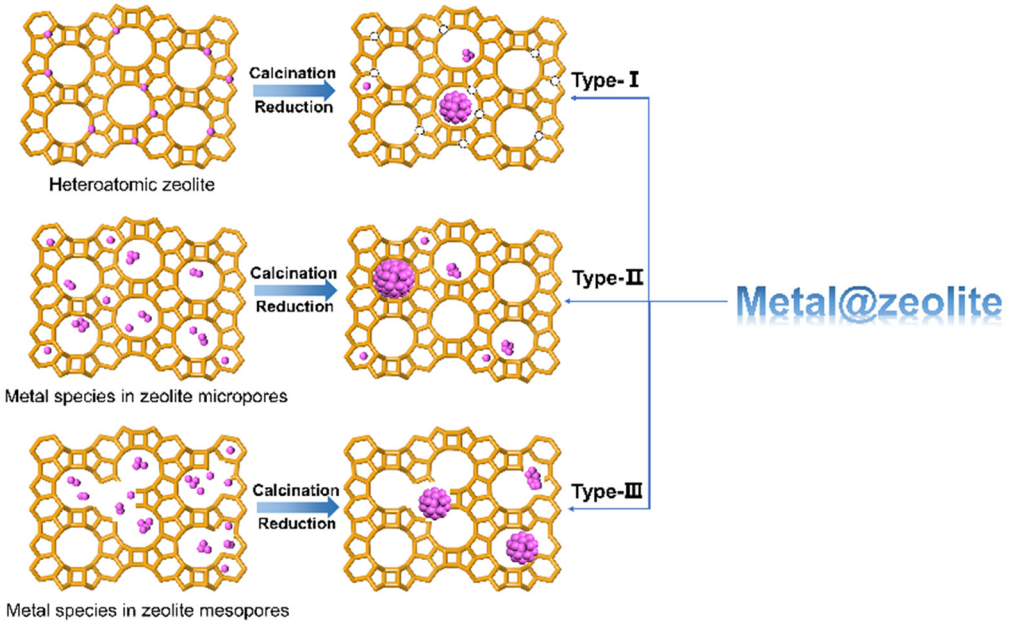

Fig. 1 Three typical types of metal@zeolite.

Ion-exchanging method is an effective route to obtain highly dispersed metal clusters within zeolite micropores but only small metal hydrated ions (*e.g.*, $[Ag(H_2O)_2]^+$ (ref. 60) and $[Cu(H_2O)_4]^{2+}$ (ref. 61)) suitable for diffusion throughout zeolites are used. The exchanging capability of zeolite is determined by its content of framework Al species, and metal loading is sensitive to the ratio of framework silicon to aluminum (Si/Al).[62] Thus, low silica zeolite (with a low Si/Al ratio) with large aperture size (*i.e.*, 10-member ring (10-MR) MFI zeolite and 12-MR FAU, MOR, and BEA zeolite) is frequently reported for preparing zeolite-confined metal catalysts *via* ion-exchanging. However, metal loading (<3 wt%) is generally low for the commonly used Beta and ZSM-5 zeolite with 20–200 Si/Al ratio from ion-exchanging method, and zeolite-encapsulated transition metal catalysts are rarely prepared. In recent years, the deposition–precipitation method has been proposed to prepare zeolite-encapsulated transition metal catalysts requiring a high metal loading (>5 wt%). Yan *et al.*[53] reported the synthesis of Ni@Beta catalyst with 6.5 wt% Ni loading *via* the deposition–precipitation method, in which the pH of the metal precursor solution and precipitation temperature were carefully screened.

3.1.2 Multistep post-treatment. The hierarchical zeolite from dealumination or desilication is characteristic of intracrystalline mesopores, which access large metal particles.[63] Zhang *et al.*[64] treated MOR zeolite with HNO_3 and $NaCO_3$ sequentially to produce mesopores and succeeded in encapsulating ~3.2 nm Pt particles by a simple impregnation method. Because the structure of zeolites is somewhat destroyed by dealumination or desilication treatment, further recrystallization has been developed for effective encapsulation. Ding *et al.*[65] proposed a new synthesis route to obtain ZSM-5 zeolite (MFI structure)-encapsulated Pt metal clusters, as shown in Fig. 2. Firstly, ZSM-5 zeolite was treated with alkaline solution, and the Pt nanoparticles were introduced into the intracrystalline mesopores *via* impregnation. Secondly, the gel of S-1 (MFI structure) was induced and mixed. Finally, Pt@MFI zeolite was obtained by a dry gel conversion method. Song *et al.*[66] reported a similar method to synthesize the ZnO@ZSM-5 catalyst for methanol to aromatics reaction.

Unlike hierarchical zeolites, it is difficult to obtain completely encapsulated noble metal or metal oxide clusters using small and medium pore zeolites (8-MR and 10-MR) *via* one-step post-treatment because the zeolite aperture is too small to transfer noble metal precursors. Thus, interzeolite transformation method is proposed by the transformation of large pore zeolite-encapsulated metal species to the target zeolite *via* hydrothermal conditions.[67,68] Iglesia *et al.*[69] encapsulated metal clusters (Pt, Ru, Rh) in MFI zeolite *via* the interzeolite transformation of FAU or BEA zeolites into MFI zeolites (Fig. 3). Firstly, metal clusters were encapsulated within FAU or BEA zeolite by the ion-exchanging method and sequential calcination and reduction treatment. Secondly, a suitable alkali solution and temperature were screened to convert FAU or BEA zeolite into MFI zeolite. Metal clusters with diameters of 1.3–1.7 nm were encapsulated in the MFI zeolite during the synthesis process. The interzeolite transformation strategy has also been proposed for the conversion of two-dimensional zeolite to three-dimensional zeolite (2D-to-3D zeolite transformation) while encapsulating the metal species.[57] Shamzhy *et al.*[43] incorporated small Pt nanoparticles into the MWW zeolite *via* this strategy. The layered 2D MWW zeolite precursors were prepared by the hydrothermal synthesis method and subsequently swelled by the aid of organic surfactant hexadecyltrimethylammonium ($CTMA^+OH^-$). During the swelling process, Pd precursors were added and 3D MWW zeolite-encapsulated Pd clusters were realized by a simple

Table 1 Summary of metal species encapsulation *via* several techniques and their catalytic performance

Zeolite encapsulated metal sample	Metal particle size (nm)	Synthesis method	Reaction	Reaction condition	Catalytic results	Ref.
Pt@S-1	4.5	*In situ* hydrothermal synthesis	Propane dehydrogenation	T = 600 °C; WHSV = 1.7 h^{-1}; C_3H_8/N_2 = 5/16 mL min^{-1}; 12 h	$Con_{C_3H_8}$ = 5.0%; $Sel_{C_3H_6}$ = 58%	42
PtZn@S-1	1.4	*In situ* hydrothermal synthesis	Propane dehydrogenation	T = 600 °C; WHSV = 3.6 h^{-1}; C_3H_8/N_2 = 10/30 mL min^{-1}; 58 h	$Con_{C_3H_8}$ = 43.2%; $Sel_{C_3H_6}$ = 95.5%;[a] k_d = 0.017 h^{-1}	37
Pd@MWW	1.14	Interzeolite transformation	Hydrogenation of 3-nitrotoluene	T = 100 °C; 3 bar H_2; 3-nitrotoluene (3-NT) : *n*-hexane : 3-nitrotoluene = 7.5 : 35 : 0.7 mL; 1 h	$Con_{3\text{-NT}}$ = 49%; $Sel_{m\text{-toluidine}}$ ~100%; reaction rate = 9.6 $mol_{3\text{-NT}}\ g_{Pd}^{-1}\ h^{-1}$	43
Pd@S-1-in-K	1.8	*In situ* hydrothermal synthesis	Decomposition of formic acid	T = 50 °C; formic acid (FA) : sodium formate (SF) = 1 : 1	[b]TOF = 3027 h^{-1}; E_a = 39.2 kJ mol^{-1}	44
$PdNi(OH)_2$@S-1	1.7	*In situ* hydrothermal synthesis	Decomposition of formic acid	T = 60 °C; without additive	[b]TOF = 1879 h^{-1}; E_a = 52.4 kJ mol^{-1}	45
Pd@Beta	2.12	*In situ* hydrothermal synthesis	*N*-Heptane hydroisomerization	T = 250 °C; WHSV = 2.0 h^{-1}; P = 4.0 MPa, H_2/*n*-heptane molar ratio = 6.64	$Con_{n\text{-heptane}}$ = ~100%; $Sel_{isomerization}$ = 30%	46
Ni@ZSM-5	10	Recrystallization	CO_2 methanation	T = 450 °C; GHSV = 60 000 mL $g_{catalyst}^{-1}\ h^{-1}$; $H_2 : CO_2$ = 4 : 1; 1 h	Con_{CO_2} = 49%; Sel_{CH_4} = 93%	47
Pd@SOD	0.8	*In situ* hydrothermal synthesis	Semi-hydrogenation of acetylene	T = 150 °C; GHSV = 30 000 h^{-1}; $H_2 : C_2H_2$ = 10 : 1; 15 h	$Con_{acetylene}$ = 99.8%; $Sel_{ethylene}$ = 94.5%	32
Pt@H-ZSM-5	—	Dry-gel synthesis	Furfural to valeric acid (VA) and ethyl valerate (EV)	T = 140 °C; 41 bar H_2; 0.5 mmol furfural; 5 mmol EtOH and 1.5 mL cyclohexane; 24 h	$Con_{furfural}$ = ~100%; Sel_{VA+VE} = 86%	27
Pd@S-1	6.9	Dry-gel synthesis	Furfural hydrogenation	T = 250 °C; 5 wt% furfural (mass ratio of furfural/*n*-butyl alcohol at 1 : 19); feed rate at 0.5 mL h^{-1}; 10% H_2/Ar at a rate of 10 mL min^{-1}	$Con_{furfural}$ = 91.3%; Sel_{furan} = 98.7%	48
MnO_x@S-1	10	*In situ* hydrothermal synthesis	Oxidative cyanation of toluene to benzonitrile	T = 160 °C; 1.5 MPa O_2; 28 mmol toluene; and 0.5 mmol urea; 4 h	TOF = 32.5 h^{-1}; $Y_{benzonitrile}$ = 88.6%	49
PtO_x@LTL	Atomically-dispersed	Ion-exchanging	CO oxidation	T = 150 °C, 1% CO; and 5% O_2 in He	TOF = 0.72 h^{-1}	50

[a] $k_d = [\ln(1 - Con_{Final})/Con_{Final} - \ln(1 - Con_{Initial})/Con_{Initial}]/t$, where Con_{Final} and $Con_{Initial}$ are the final and initial conversions of the PDH reaction, respectively, t is the duration of a PDH reaction in hour, k_d is the deactivation constant. [b] TOF is the total turnover frequency when the conversion of FA reaches 100%.

calcination progress. Moreover, the same strategy was also used for the encapsulation of Au subnanoclusters.[70] In addition to CTMA$^+$OH$^-$, 1-octanethiol was also incorporated into the swelling mixture. Benefiting from the strong interaction of the Au–S bond, the Au loading in Au@MCM-22-L samples was increased to 0.11 wt%, which was higher than that of Au@MCM-22-S (0.025 wt% Au loading, prepared in the absence

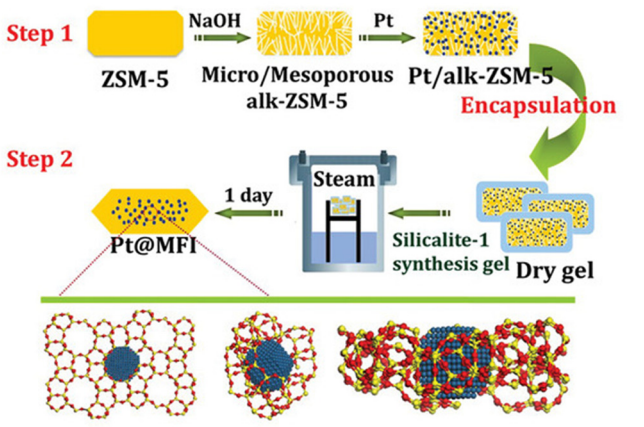

Fig. 2 Scheme of synthesis of MFI zeolite-encapsulated Pt nanoparticles.[65] Reprinted with permission from American Chemical Society, copyright 2015.

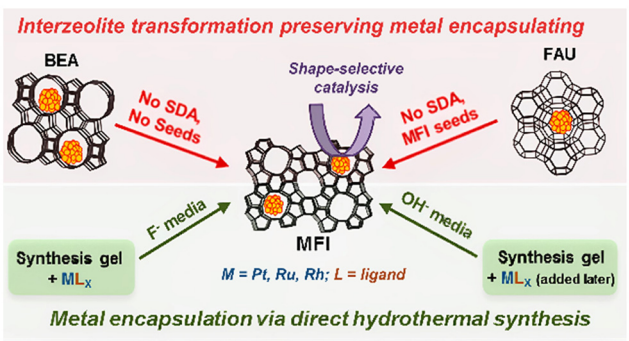

Fig. 3 Schematic representation of interzeolite transformations progress.[69] Reprinted with permission from American Chemical Society, copyright 2014.

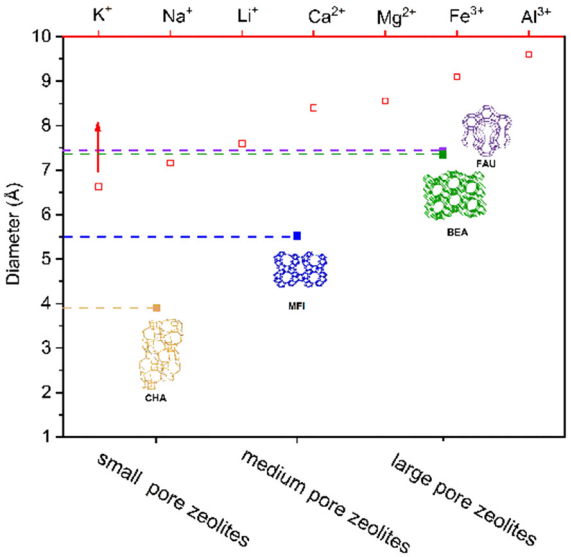

Fig. 4 The relationship between the diameter of metal hydrated ions and the pore size of zeolites.

of 1-octanethiol). However, it should be noted that the high Au loading in Au@MCM-22-L can lead to the distribution of both subnanometric Au clusters and Au nanoclusters (~1 nm) in MCM-22 zeolite micropores.

3.2 *In situ* method

3.2.1 *In situ* hydrothermal synthesis. The *in situ* hydrothermal synthesis method is frequently reported for the encapsulation of metal and metal oxide clusters within small pore and medium pore zeolites. As shown in Fig. 4, we can clearly see that the diameter of hydrated metal complex is always larger than the aperture size of small and medium pore zeolites; thus, the metal precursor is difficult to diffuse throughout the zeolite aperture.[71,72] The *in situ* hydrothermal synthesis method shows that the success of encapsulation benefits from no diffusion barrier for metal precursors through zeolite apertures during crystallization. However, incorporating bulk metal hydroxides into the zeolite cages is implausible when the fast precipitation of unstable metal cations in alkaline aluminosilicate gel occurs because the size of the bulk hydroxide precipitates is much larger than the zeolite aperture and cage size.[73] Therefore, various stabilization strategies for the metal precursors without precipitation or aggregation prior to zeolite crystallization are focused on and developed.

Ammonia and organic amines were firstly proposed as good ligands for stabilizing metal precursors during zeolite encapsulation.[74] In 1980s, Davis *et al.*[74,75] prepared LTA zeolite-encapsulated Ru nanoparticles using $[Ru(NH_3)_5Cl]Cl_2$ as precursors *via* hydrothermal synthesis. Iglesia *et al.*[71,72,76] systematically developed the chemistry of this encapsulation method. Ammonia and organic amines ligands were found to be suitable for encapsulating most noble metal clusters within a series of small-pore zeolites (SOD, GIS, ANA, *etc.*).[71] Yu *et al.*[77] further developed this method for encaging Rh metal single atoms in S-1 zeolite (Rh@S-1-H) using ethylenediamine as the ligand (Fig. 5). The Rh@S-1-H precursor received from the *in situ* hydrothermal synthesis method was treated by hydrogen reduction without calcination for template removal. Ethylenediamine (en) and tetrapropyl ammonium (TPA^+) templates were gradually decomposed during the reduction progress, serving as protective agents to inhibit the aggregation of Rh species. Cs-corrected high-angle annular dark-field STEM (HAADF-STEM) and high-resolution transmission electron microscope (HR-TEM) results revealed that Rh atoms in Rh@S-1-H were uniformly distributed in sinusoidal 5-MRs of the S-1 zeolite with atomic dispersion. Yu *et al.*[37] also developed such a method to prepare ultrasmall Pt–Zn bimetallic clusters within the S-1 zeolite.

Beside ammonia and amines ligands, mercapto-based ligands with stronger complexing ability to metal cations were

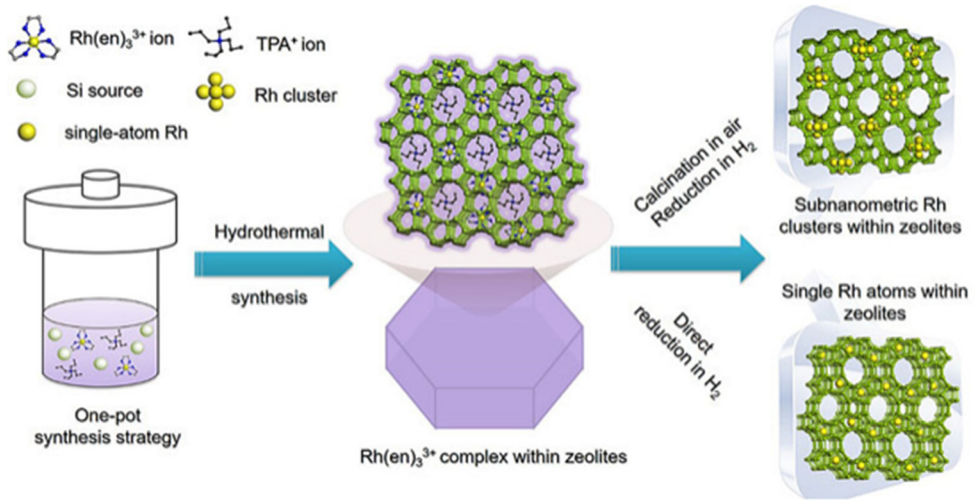

Fig. 5 Schematic of the synthesis of the Rh@S-1 catalyst.[77] Reprinted with permission from Wiley-VCH, copyright 2019.

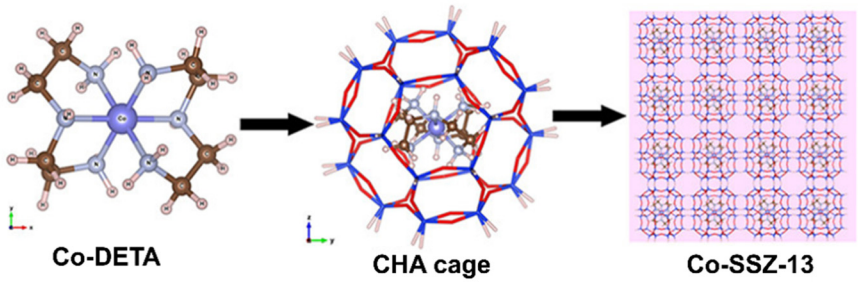

Fig. 6 Positions of Co-DETA complex within the CHA framework.[83] Reprinted with permission from American Chemical Society, copyright 2018.

developed for some unstable metal cations (*i.e.*, Au^{3+} and Ag^{+}) in alkali solution. 3-Mercaptopropyl-trimethoxysilane (MPS) is widely employed as a bifunctional ligand, in which the mercapto group (–SH) can react with metal species to form stable metal–sulfur adducts, and alkoxysilane groups undergo hydrolysis and form Si–O–Si or Si–O–Al bonds in alkaline media, thereby promoting nucleation around the metal precursors to form an encapsulation structure.[78,79] Li *et al.*[80] confined small sized Ag clusters into the S-1 zeolite with MPS as a ligand (Ag@S-1). HR-TEM and HAADF-STEM results showed that the encapsulated Ag clusters were uniformly distributed in the S-1 zeolite with an average size of ~1 nm.

In some case, the ligands stabilizing metal ions may interfere the structure-directing role of templates, leading to difficulty in zeolite crystallization.[69] Thus, bifunctional ligands with stabilizing metal ions and directing zeolite crystallization were proposed.[81] Xiao *et al.*[82] developed the use of metal–amine complex as structure directing agent (SDA) and metal precursors for zeolite-encapsulated metal clusters. As shown in Fig. 6, cobalt-diethylenetriamine complex (Co-DETA) were prepared as the SDA for SSZ-13 zeolite (CHA structure),[83] in which Co-DETA is self-consistent with the geometry of CHA cage and can also stabilize Co cations without precipitation during hydrothermal synthesis. Li *et al.*[84] also reported a similar synthesis strategy to synthesize Ni@CHA catalyst using Ni-DETA complex as SDA and metal precursors.

3.2.2 Dry-gel synthesis. The incorporation of metal species into zeolite structures can be easily achieved by the dry-gel synthesis method. Ye *et al.*[85] prepared S-1 zeolite-encapsulated Pd nanoparticles using the dry-gel synthesis method. First, Pd precursors were introduced into a sol for S-1 zeolite containing silica sol and tetrapropylammonium hydroxide (TPAOH), and the dry gel was composed by heating treatment at 80 °C. Then, the as-prepared dry gel was transferred into an autoclave and crystallized at 180 °C for 24 h. Pd@S-1 zeolite was obtained by subsequent calcination and reduction treatment. TEM and HAADF-STEM images showed that the size distribution of Pd nanoparticles of the Pd@S-1 was mainly in the range of 0.7–3.1 nm, with mean sizes of ~1.1 nm. Cho *et al.*[26] developed a polymer-assisted dry-gel synthesis method for ZSM-5 zeolite encapsulating metal anions, as shown in Fig. 7. Polydiallydimethylammonium chloride (PDDA) was prepared to stabilize metal anions and served as the linking agent with aluminosilicates. PDDA also acted as soft templates for the intramesopores for ZSM-5 zeolite, and the metal clusters could be encapsulated within the mesopores. The TEM images and CO chemisorption indicated that the Pt particles were highly dispersed in the ZSM-5 crystals with an average

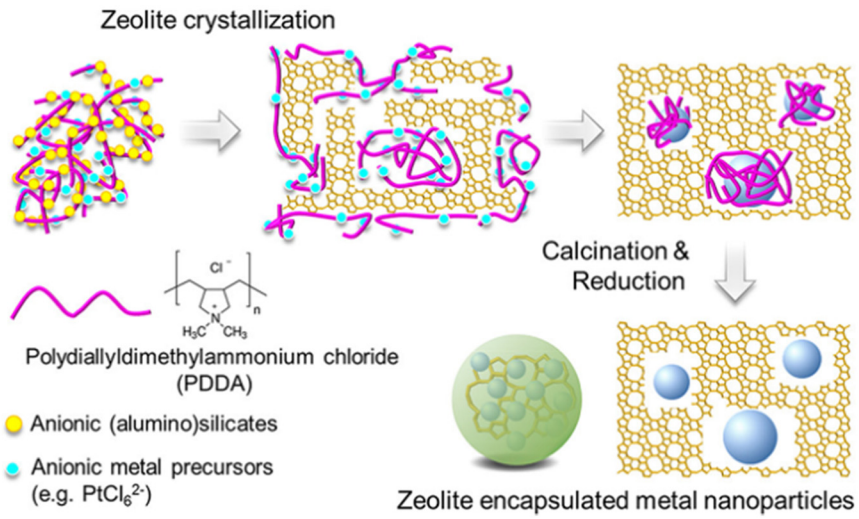

Fig. 7 Synthesis of the polymer-assisted Pd@HZSM-5 catalyst.[26] Reprinted with permission from American Chemical Society, copyright 2018.

size of ~5.4 nm. Oxidation reactions with different sized substrates indicated that >90% Pt nanoparticles were encapsulated in the ZSM-5 zeolite matrix.

3.2.3 Other *in situ* synthesis method. In addition to the commonly used *in situ* hydrothemal and dry-gel synthesis methods, some unique *in situ* synthesis methods have been developed. Generally, the *in situ* hydrothermal or dry-gel synthesis methods are slow to crystallize and come with a high cost in terms of time and energy. Liu *et al.* reported an ultrafast *in situ* synthesis route to encapsulate Pt and Sn nanoclusters into a high-silica ZSM-5 zeolite.[86] In the synthesis progress, $Pt(NH_3)_2(NO_3)_2$ and $SnCl_4$ were chosen as Pt and Sn precursors, respectively, and added into an aged silica-alumina gel for synthesizing high silica ZSM-5. After stirring and sonication, the homogenized mixture was transferred into a tubular reactor and then subjected to hydrothermal synthesis at 190 °C for 5 min. Finally, Pt/Sn-ZSM-5 was obtained by subsequent calcination and reduction treatment. Zhang *et al.*[87] used a dual-template method to prepare a finned MFI zeolite to confine PtZn clusters (<1 nm). This unique finned structure ensured a short diffusion length and improved the diffusion rate, which contributed to a high activity (17.0 $mol_{C_3H_6}$ mol_{Pt}^{-1} s^{-1}) and a low deactivation constant of 0.0017 h^{-1} in the propane dehydrogenation (PDH) reaction. Recently, our group[88] developed an *in situ* two-stage hydrothermal synthesis method to encapsulate ultrasmall Ru clusters (~1 nm) into a high-aluminum ZSM-5 zeolite without using organic ligands for Ru cations. In the synthesis progress, the aluminosilicate gel was first precrystallized at 100 °C to produce MFI structural units, and then introduced $RuCl_3$ solution and carried out the crystallization at a relatively high temperature of 170 °C. The preliminary nucleation step can provide sufficient zeolite nuclei and efficiently prevent the negative impact of the metal precursor on the assembly of the zeolite under the hydrothermal conditions.

4 Characterization of zeolite-encapsulated metal species

Because of the confinement effect within zeolite micropores, zeolite-encapsulated metal or metal oxides show small size, even in subnanometer or atomic scale. Moreover, the geometric and electronic properties of encapsulated metal species are complex because of the strong metal-framework interaction. Therefore, identifying metal particles confined in zeolites is challenging. In this section, the recent advances in characterization methods for distinguishing encapsulation, determining metal size, and identifying the coordination environment and electronic structures of metal entities confined in zeolites are discussed.

4.1 Structural characterization

X-ray diffraction (XRD) pattern is commonly employed to determine the topology of zeolite and estimate the formation of large metal species.[89,90] The signal of metal species in XRD patterns indicates the failure in the encapsulation of metal species within zeolite micropores. TEM characterization is another common tool to determine the size of metal species and distinguish large metal aggregates not smaller than 2 nm.[91] The large metal particles far beyond the zeolite micropore size can be directly ascribed to aggregates at the external surface of the zeolite. Thus, TEM images combined with energy dispersive spectroscopy (EDS) mapping were frequently reported to provide the possible evidence of encapsulated metal species within zeolite micropores, in which no metal species could be direct observed by TEM images but can be distinguished *via* EDS.[92] In recent years, HAADF-STEM has been developed as a reliable technique to analyze subnanometric metal clusters and even isolated atoms, and has also been developed for detecting zeolite-encapsulated metal species. Li *et al.*[93] succeeded in detecting 1–2 nm highly dispersed Pd particles in ZSM-5 zeolite *via* HAADF-STEM, and they further employed Cs-corrected HAADF-STEM to distinguish the location of Pt particles within Y zeolite crystals.[94] Pt particles were found to be atomically-dispersed and located in the 6-MR shared by sodalite cages and supercages of Y zeolite. Moreover, EDS and/or electron energy loss spectroscopy (EELS) have been used to identify and illustrate the dispersion of metal species. Sun *et al.*[45] prepared S-1 zeolite-encapsulated Pd and $Ni(OH)_2$ species with subnanometric Pd–$Ni(OH)_2$ clusters (Pd–$Ni(OH)_2$@S-1). As shown in Fig. 8, the EDS spectral mapping images clearly showed that Pd and Ni elements were uniformly distributed in almost the same position, indicating the formation of bimetallic clusters. Cs-corrected HAADF-STEM further revealed that the Pd and $Ni(OH)_2$ clusters may be in the intersectional spaces between the straight and sinusoidal channels of the MFI structure since the straight channels were empty and intact.

At present, Cs-corrected HAADF-STEM has been widely used to directly observe the isolated atoms and clusters for catalytic materials. It is worth noting that the validity of the encapsulation information is limited by the local observation and the heterogeneity of samples. In addition, zeolites are usually quite sensitive to the electron beam, and the structure could be partially or completely damaged in HAADF-STEM tests.[95,96] Recently, integrated differential phase contrast-STEM (iDPC-STEM) is developed to provide atomically-resolved images of light and heavy elements and to directly image electron beam-sensitive materials with optimal signal-to-noise ratio without damaging the sample. Liu *et al.*[97] used the iDPC-STEM technique to study the location of Mo species in the Mo@ZSM-5 zeolite. The iDPC-STEM images clearly showed that isolated single-Mo atoms were in the micropores of ZSM-5. Another example is the use of iDPC imaging techniques to visualize the evolution of single-site Ir atoms to stabilized subnanometric Ir clusters in the pure-silica MWW zeolite.[98] With the aid of iDPC-STEM, atomically-dispersed Ir metal in the 10-MR window connecting the neighboring 12-MR supercages was observed

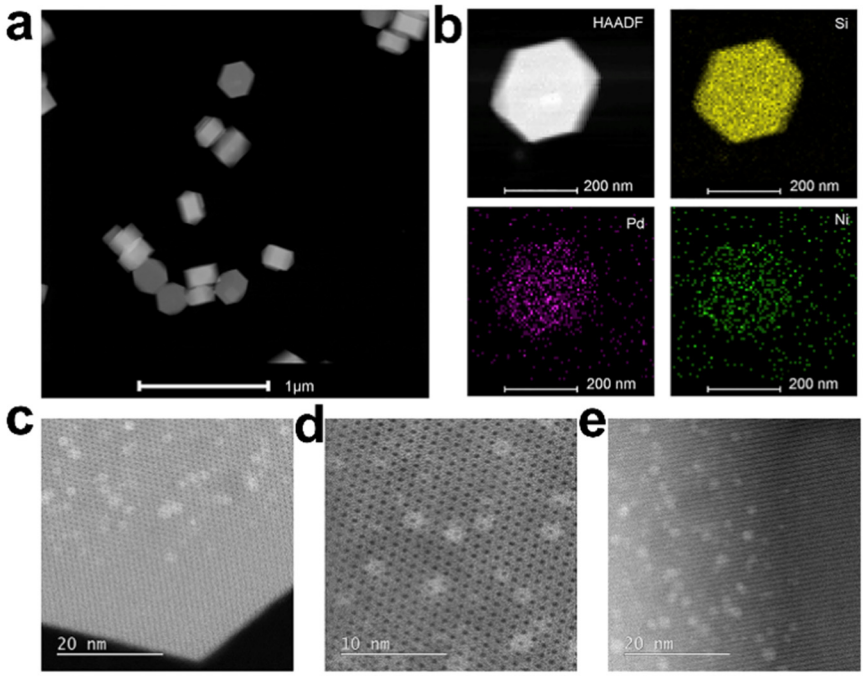

Fig. 8 (a) STEM and (b) HAADF-STEM image of the 0.8Pd0.2Ni(OH)$_2$@S-1 catalyst and the corresponding EDS mapping images for Si, Pd, and Ni elements; (c and d) Cs-corrected HAADF-STEM images of the 0.8Pd0.2Ni(OH)$_2$@S-1 catalyst viewed along the *b*-axis orientation with low and high magnification and (e) viewed along other orientation.[45] Reprinted with permission from Elsevier Inc, copyright 2017.

in the MWW zeolite as well as the formation of subnanometric Ir clusters (0.4–0.8 nm) after high temperature reduction treatment. In fact, the above TEM or STEM measurement are used to determine the size distribution and average size of metal particles. Generally, the clusters are regarded to be spherical in shape, and the surface-area-weighted cluster diameter (d_{TEM}) could be calculated. The as-calculated diameter should be further confirmed by chemisorption. Chemisorptive titrations of metal surfaces with CO or H_2 give metal dispersion, and the dispersion corresponds to mean cluster diameter (d_{chem}) calculated by assuming spherical crystallites and the density of each bulk metal. The comparison between the cluster diameter determined by chemisorption (d_{chem}) and by transmission electron microscopy (d_{TEM}) is significant for the encapsulated metal clusters. For example, ultrasmall metal clusters within small pore zeolites, such as SOD or GIS zeolites, are difficult to be distinguished by TEM experiments so that these clusters cannot be included in cluster size calculation using TEM measurement, which results in the overestimation of d_{TEM}. On the other hand, the dispersion calculated by chemisorption is influenced by the accessibility of adsorbing probe molecular onto the metal surface. When the zeolite cages or channels are partly occupied by metal clusters, the size of the molecular probe also could influence the titration of metal surface owing to the limit of the residual space in the zeolite cages or channels. Taking Na-form LTA zeolite-encapsulated Pt metal clusters as an example,[71] the aperture (0.41 nm) of α-cages allows the diffusion of CO (kinetic diameter: 0.39 nm) to access Pt clusters but ~3 times lower dispersion from CO chemisorptions (0.21) was obtained compared to hydrogen (kinetic diameter: 0.29 nm) chemisorptions (0.75). This means that CO gas could not titrate all Pt metal surfaces within α-cages and also believe that it is difficult to titrate the entire metal surface even by hydrogen atoms (diameter: 0.11 nm), resulting in a little lower dispersion than obtained by actual dispersion. Anyway, a good agreement between d_{chem} and d_{TEM} indicates that the metal clusters are distributed narrowly within zeolite micropores.

X-ray absorption (XAS) is a powerful technique for realizing global information on the dispersion and coordination environment of metal species confined in zeolite crystals. For XAS characterization, based on the formation mechanism and data processing method, the analysis of XAS results is usually divided into two distinct parts: X-ray absorption near edge structure (XANES) and extended X-ray absorption fine structure (EXAFS). XANES focuses on the region before the absorption edge −50 eV after the absorption edge and has a "fingerprint effect", which can provide information such as the electronic state and valence state of confined metal atoms.[99] EXAFS pays attention to 50 eV after the absorption edge −1000 eV, and the morphology is a continuous slow weak oscillation.[100] Fitting EXAFS can provide the information on the structure, including the coordination numbers, bonding distances, and thermal perturbation of confined metal species. Li *et al.*[101] succeeded in distinguishing encapsulated Co ions in Y zeolite by Co K-edge XANES and EXAFS spectroscopy, as shown in Fig. 9. The XANES spectra showed that the energy absorption edge

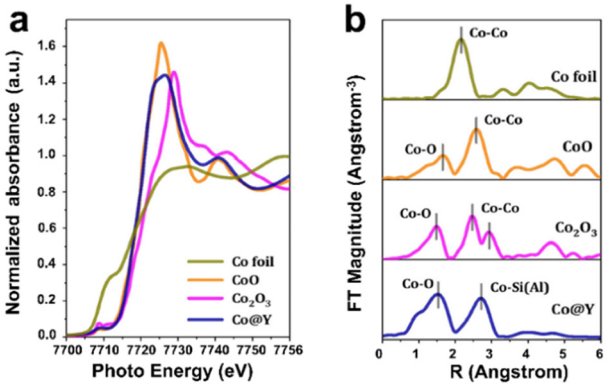

Fig. 9 XAS characterization of the Co@Y sample. (a) Co K-edge XANES spectra; (b) FT k^2-weighted EXAFS spectra.[101] Reprinted with permission from American Chemical Society, copyright 2022.

of Co@Y was between CoO and Co_2O_3, revealing that the valence of Co species was in the range from +2 to +3. The Fourier-transform (FT) k^2-weighted EXAFS spectra of Co@Y exhibited two prominent peaks at ~2.0 Å and ~3.3 Å, corresponding to the first shell of the Co–O path and the second shell of the Co–Si(Al) path, respectively. Then, the absence of the Co–Co path indicated that all the Co atoms were singly dispersed.

It should be noted that ultrasmall metal clusters (*i.e.*, subnanometric metal clusters) are sensitive to environmental changes, and the state of the metal clusters changes dynamically during the catalytic reaction. Therefore, *in situ* or operando XAS measurements have attracted increasing focus. Time-resolved scanning XAS under operando condition was employed to study the evolution of encapsulated Cu species during the selective catalytic reduction (SCR) of NO by NH_3.[102] According to XAS spectra, at low temperature (<250 °C) under SCR conditions, the activity of Cu-SSZ-13 was derived from the formation of $Cu^{II}(NH_3)_4$ species by NH_3 adsorption on Cu sites. During the SCR reaction, $Cu^{I}(NH_3)_2$ species increased with the simultaneous attenuation of $Cu^{II}(NH_3)_4$ species, and the re-oxidation of $Cu^{I}(NH_3)_2$ was the rate-limiting step. However, NH_3 inhibited the re-oxidation of Cu(I), leading to a decrease in their low-temperature activity for the SCR reaction. The *in situ* or operando XAS provides a new and significant chance to clarify the reaction mechanism for the rational design of more active catalysts.

4.2 Surface characterization

X-ray photoelectron spectroscopy (XPS) is a routine but effective tool to estimate the success of encapsulation. Beside the electronic states of the surface element of zeolite-containing metal samples, the surface concentration of elements combined with the bulk composition of the samples could give clear evidence of encapsulation. Because of the low external surface area but large micropore surface area of the zeolite samples, a lower content of metal species from XPS compared to the bulk content from elemental analysis may suggest the distribution of metal species within the zeolite micropores. As shown in Fig. 10a, the signal of Pt@Y with Pt particles confined in the Y zeolite were much less than that of Pt/Y in which most of the Pt particles were located at the external surface of the Y zeolite.[94] It should be noted that the internal information of the metal species can be obtained by etching treatment using inert gas ion bombardment. Zhao *et al.*[103] etched the Pt-containing samples using Ar^+ ion sputtering to an etching depth of about 20 nm and then performed XPS measurements (Fig. 10b). The corresponding binding energies of Pt^0, Pt^{2+}, and Pt^{4+} in Pt@Beta were higher than those of Pt/Beta, which demonstrated the strong metal–zeolite interaction in Pt@Beta.

In addition to XPS, H_2 temperature-program reduction (H_2-TPR) has been frequently included as a supplement to confirm the surface properties due to interaction between the metal and the zeolite.[104,105] It can be used to determine the reducibility and identify the types of metal species present in the zeolites. It is generally believed that the reduction temperature of isolated metal atoms is higher than that of the corresponding aggregated metal oxide nanoparticles. For example, the H_2-TPR profile of CoSiBeta had three reduction peaks located at about 280 °C, 400–600 °C, and >600 °C,

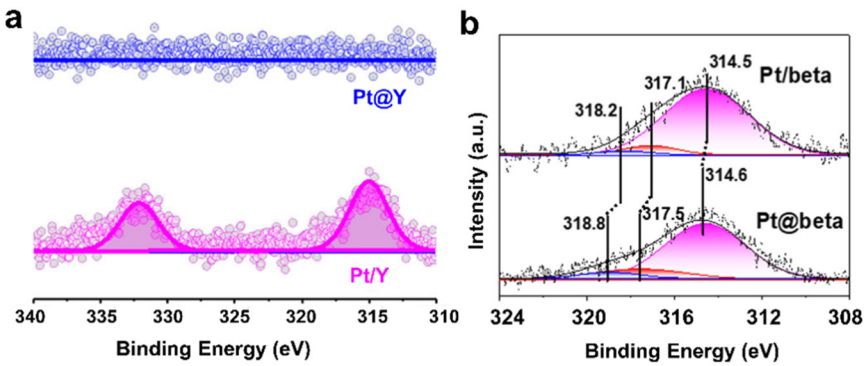

Fig. 10 (a) Pt 4d XPS of Pt@Y and Pt/Y without Ar^+ ion sputtering.[94] Reprinted with permission from American Chemical Society, copyright 2021; (b) Pt 4d XPS of Pt@Beta and Pt/Beta with Ar^+ ion sputtering.[103] Reprinted with permission from Wiley-VCH, copyright 2021.

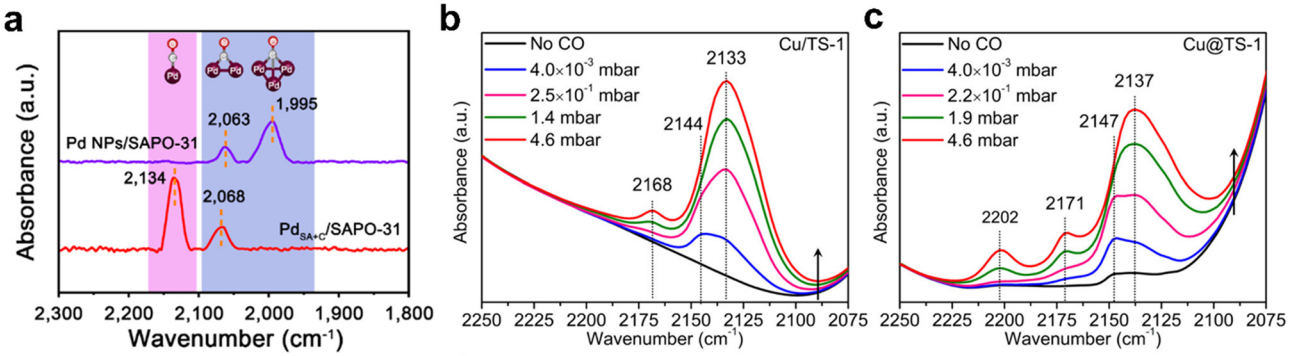

Fig. 11 (a) FTIR-CO spectra of Pd@SAPO-31 and Pd/SAPO-31.[108] Reprinted with permission from Springer Nature, copyright 2021; FTIR-CO spectra of (b) Cu/TS-1 and (c) Cu@TS-1.[109] Reprinted with permission from American Chemical Society, copyright 2021.

which could be attributed to the reduction of superficial CoO_x on the Si-Beta support, CoO_x in the T sites of Si-Beta, and isolated Co ions, respectively.[106]

The chemisorption of small probe molecular has been developed to test the geometric and electronic structure of zeolite-encapsulated metal species. Specially, Fourier transform infrared spectroscopy of CO (FTIR-CO) is frequently reported because CO is extremely sensitive to the geometric and electronic structure of the metal site. For the CO adsorption on metal sites confined in zeolites, it typically exhibits multiple binding states, providing information on the oxidation and coordination state.[88,107] Lu *et al.*[108] used low-temperature FTIR-CO to study the Pd particles confined in the SAPO-31 zeolite (Fig. 11a). For Pd@SAPO-31, two peaks were observed at 2134 and 2068 cm^{-1}, corresponding to the linear-adsorbed CO on isolated Pd sites and bridge-adsorbed CO on small Pd clusters, indicating the co-existence of Pd single atoms and small Pd clusters confined within the zeolites. FTIR-CO also can be employed to determine the electronic properties of metal species. The peak shows blue- or red-shifted due to the difference in the strength and nature of interactions between the metal species and zeolites, which is useful for clarifying the properties of metal species. Cao *et al.*[109] studied the state of Cu species within the TS-1 zeolite (Fig. 11b and c). For Cu/TS-1, three CO adsorption peaks at 2168, 2144, and 2133 cm^{-1} were ascribed to the symmetric vibrations of Cu^+–$(CO)_2$, antisymmetric vibrations of Cu^+–$(CO)_2$ and Cu^+–CO species, respectively. The spectra of Cu@TS-1 showed slight blue shifts for Cu^+–CO at 2137 cm^{-1}, Cu^+–$(CO)_2$ at 2147 and 2171 cm^{-1}, demonstrating electron withdrawal from Cu by the zeolite framework, confirming the strong metal–zeolite interaction in Cu@TS-1.

4.3 Encapsulation fraction determination *via* probe molecular titration

The metal species encapsulated within zeolites show many advantages in comparison to conventional metal deposited on supports because the well-defined and well-ordered microporous void structure of the aluminosilicate framework of zeolites stimulates a uniform metal cluster size within the zeolites and initiate shape and size selectivity for reagents, intermediates, and products of catalytic reactions. The fraction of metal clusters encapsulated inside the zeolites can be tested by suitable probe molecular titration reaction. Iglesia *et al.*[71] prepared LTA zeolite-encapsulated noble metal clusters (Pd, Pt, Rh, *etc.*) and used the turnover rates (TOR) for the hydrogenation of alkenes with different kinetic diameters (ethylene: 0.39 nm and isobutene: 0.50 nm) to represent the activity of metal clusters on NaA and SiO_2 samples. The specificity of encapsulation is reflected by the ratio of TOR values, defined as χ, for small and large reactants on clusters dispersed on NaA and SiO_2 samples. The ratio of these χ values for NaA and SiO_2 samples, defined as ϕ, reflects the diffusional constraints for access to intrazeolite clusters for a larger reactant. The ϕ value near 1 indicates that the accessibility of reagents to clusters is the same on NaA and SiO_2, and the molecules are essentially unconstrained. Larger ϕ values provide rigorous evidence for the preferential containment of active clusters within spatially-constrained micropores that can sieve reactants based on their molecular size. Pd/LTA, Pt/LTA, and Rh/LTA gave ϕ value much larger than 1 (8.3, 7.5, 82.9, respectively) confirming that Pd, Pt, and Rh clusters reside predominantly within LTA voids.

As shown in Fig. 12, He *et al.*[107] used the hydrogenation of toluene (0.3 nm) and 1,3,5-triisopropylbenzene (TIPB, 0.85 nm) to test the encapsulation fraction of FAU zeolite-encapsulated Ru catalysts. The fraction of encapsulation was reflected by the difference in the turnover frequency (TOF) values over Ru@FAU and Ru/SiO_2 samples. We previously reported the same method to determine the proportion of Ru clusters within the ZSM-5 zeolite at 92% for Ru@ZSM-5, confirming that most Ru clusters (~1.3 nm) are confined in the micropores of the ZSM-5 zeolite.[88] Cho *et al.*[110] developed the oxidation of cyclohexanol (Cy6-ol, 0.60 nm) and cyclododecanol (Cy12-ol, 0.84 nm) with *tert*-butyl hydroperoxide in acetonitrile as a model reaction to determine 90% encapsulation fraction of Pt nanoparticles within the BEA zeolite.

Currently, there is still no effective method for accurately identifying the encapsulation fraction metal species within the zeolite. Therefore, the results from different characterizations should be synchronized together to better understand the properties of zeolite-encapsulated metal catalysts.

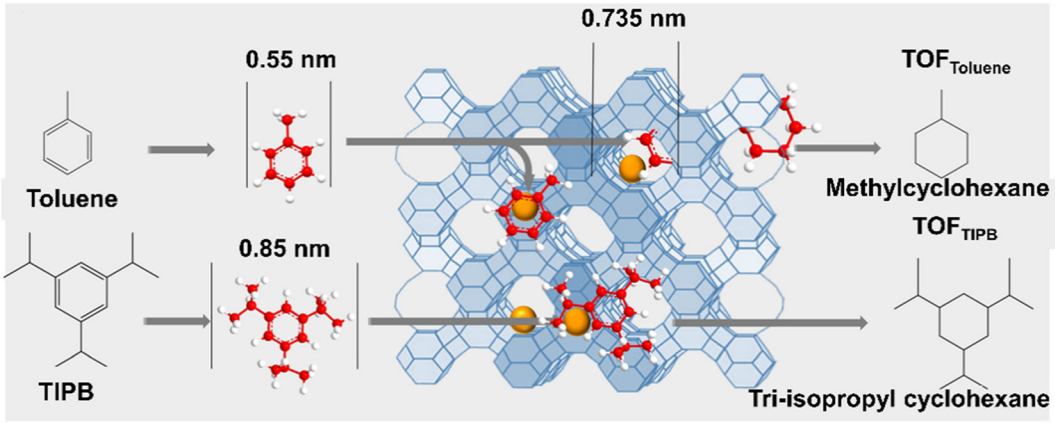

Fig. 12 Diagram of hydrogenation tests with toluene and TIPB as the probing molecules.[107] Reprinted with permission from Wiley-VCH, copyright 2021.

5 Catalytic consequence

The encapsulation of metal species within zeolites is an attractive route to contain and maintain small and uniform metal clusters, to protect them against sintering and poisoning, and to select reactants, products, and transition states in catalytic reactions. However, the confinement of metal species within zeolites may also increase the diffusion barrier of the reactant or product throughout the zeolite aperture, leading to a somewhat decreasing reaction rate.[111] Again, the confinement inevitably sacrifices some acid site *via* the interaction between the metal species with the zeolite framework.[112] These together make the catalytic consequence of the zeolite-encapsulated metal catalysts complex, which is varied with the reaction conditions. In this section, we mainly discuss the catalytic consequence of metal species confined in zeolites in terms of activity, selectivity, and stability during catalytic reactions.

5.1 Activity

5.1.1 Na-type and pure silica zeolite. Zeolite-encapsulated metal species possess small particle size with high coordination unsaturation, which is characteristic of high reactivity. Sun *et al.*[77] confined single Rh atoms into S-1 zeolite using $[Rh(NH_2CH_2CH_2NH_2)_2]Cl_3$ as metal precursors. The as-obtained catalyst showed impressive activity for ammonia borane hydrolysis with a TOF value of 432 mol_{H_2} mol_{Rh}^{-1} min^{-1}, which was more than 2- and 6-times higher than that of the S-1 zeolite-encapsulated Rh clusters (<1 nm, 195 mol_{H_2} mol_{Rh}^{-1} min^{-1}) prepared by calcination–reduction procedure and S-1 zeolite-impregnated Rh particles (>5 nm, 65 mol_{H_2} mol_{Rh}^{-1} min^{-1}), respectively. The superior activity was attributed to the single-atom Rh metal with high reactivity.

The encapsulation of metal species within zeolites involves the inherent problem of mass transfer limitation in micropores, which is detrimental to the efficiency of the catalytic reaction.[113,114] To address this point, Peng *et al.*[39] employed a single crystal intramesopore MFI zeolite to encapsulate Pd nanoparticles (Pd@IM-S-1) *via* a facile *in situ* mesoporogen-free strategy (Fig. 13a). Firstly, Pd@SiO_2 was prepared by a reversed-phase microemulsion method and then used as a precursor for the synthesis of Pd@IM-S-1 through the *in situ* dry-gel synthesis process. In the synthesis process, the amorphous SiO_2 shell of Pd@SiO_2 will be converted to S-1 shell through continuous heating. FIB aberration-corrected bright field TEM (FIB-AC-BF-TEM) and FIB aberration-corrected high-angle annular dark-field TEM (FIB-AC-HAADF-TEM) images of Pd@IM-S-1 demonstrated that many intramesopores with a mean size of ~21.9 nm were present in the zeolite crystals, and Pd nanoparticles were confined within the IM-S-1 shell. As shown in Fig. 13b and c, Pd@IM-S-1 exhibited an outstanding deep oxidation activity for methane and propane, the TOF value at 265 °C was 2- and 7-fold higher than that over the traditional S-1 zeolite-supported Pd and SiO_2-supported Pd catalysts, respectively. After five cycling tests for propane deep oxidation at 300 °C, Pd@IM-S-1 was held steady at 90% conversion while Pd/S-1 was ~20% of conversion. These results demonstrated that Pd@IM-S-1 had better activity and recyclability than Pd/S-1 because Pd@IM-S-1 contained micropores and the supernumerary intramesopores simultaneously, which can improve the mass transfer rate as well as the accessibility to Pd active sites.

5.1.2 H-type zeolite. Spillover phenomena are ubiquitous in catalysis and involve the transport of active species formed for one function to another function, which by itself does not form the active species or catalyze the reaction under the conditions of the experiment. The activated hydrogen species typically form on metal or oxide functions and then transfer to an acceptor site, such as unsaturated molecules activated by acid sites, then undergo reduction. Thus, it can be interfered that the close proximity of acid sites and metal sites promote the hydrogenation activity using H-type zeolite-encapsulated metal catalysts.[115–117] Lu *et al.*[118] prepared a series of core–shell catalysts by the epitaxial growth of ZSM-5 shell around the S-1 zeolite-supported Pd nanoparticles core with different crystallization time (Pd/S-1@ZSM-5-*x*, *x* = crystallization time (h)) (Fig. 14a). Pd/S-1@HZSM-5-*x* was

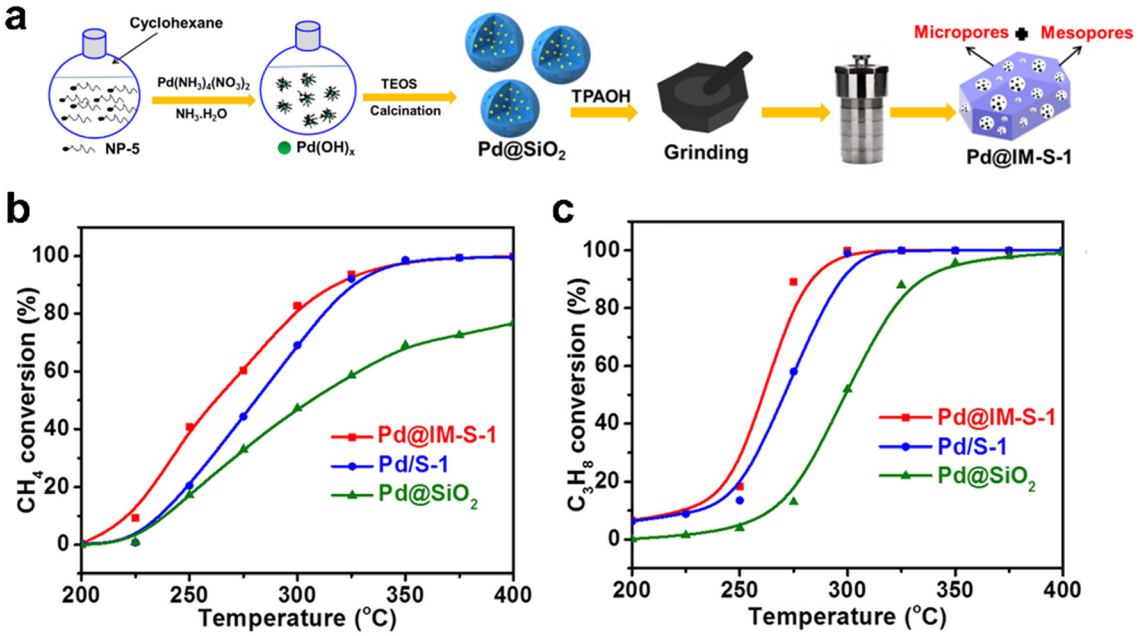

Fig. 13 (a) Schematic diagram of the synthesis of Pd@S-1 catalyst; deep oxidation performance of (b) methane and (c) propane on Pd-based catalysts (reaction conditions: WHSV = 36 000 mL $g_{cat.}^{-1}$ h^{-1}, 0.1 MPa, 200–400 °C).[39] Reprinted with permission from Springer Nature, copyright 2022.

prepared by the NH_4^+ exchange of the corresponding Pd/S-1@ZSM-5-*x*. NH_3 temperature-programmed desorption (NH_3-TPD) results showed that the strong acid amount around the Pd nanoparticles was increased with the crystallization time. The nanopore environments of zeolites could significantly affect the catalytic activity of naphthalene hydrogenation. As shown in Fig. 14b, the core–shell Pd/S-1@HZSM-5-*x* catalyst showed a super high naphthalene conversion at 6 h, in particular, the naphthalene conversion of Pd/S-1@HZSM-5-48 reached 98.3%, while the Pd/S-1 catalyst exhibited a naphthalene conversion of 5.1% under the same conditions. In addition, Pd/S-1@NaZSM-5-48 prepared by ion-exchanging with NaCl solution and Pd/[S-1@HZSM-5-48] prepared by the wet-impregnation method using S-1@HZSM-5-48 as the support were obtained to further confirm the enhancement in the hydrogenation ability of the HZSM-5 shell. The naphthalene conversion of Pd/S-1@NaZSM-5-48 (27.7%) and Pd/[S-1@HZSM-5-48] (71.5%) were much lower than that of Pd/S-1@HZSM-5-48 (96.1%) at 10 h. These results revealed that the acid support was beneficial for spillover hydrogenation and adjusting the distance between the acid sites and metal particles could further improve spillover

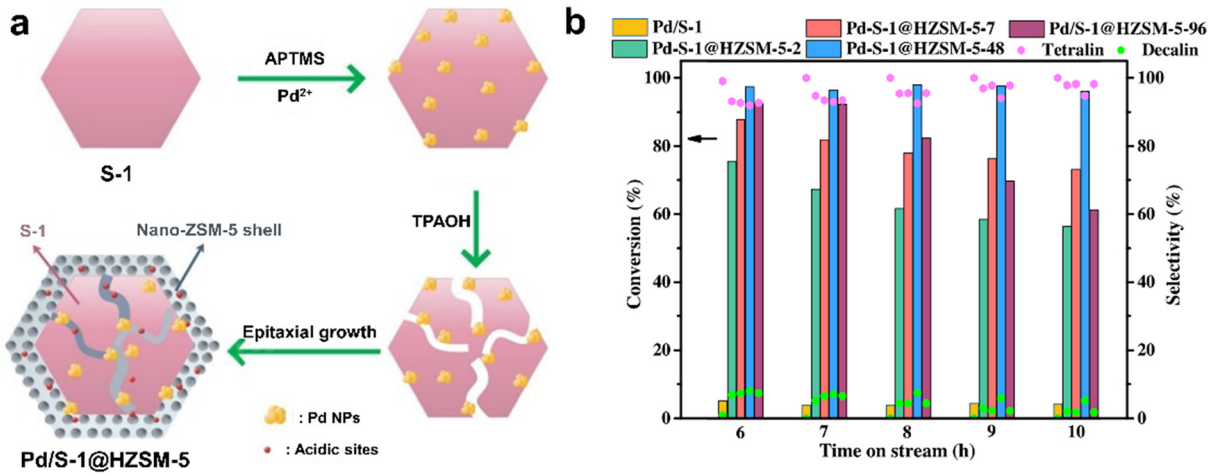

Fig. 14 (a) The preparation progress for the Pd/S-1@HZSM-5 catalyst; (b) catalytic performances of naphthalene hydrogenation over different catalysts (reaction conditions: WHSV = 1.3 h^{-1}, H_2/feed = 750, 4 MPa H_2, 280 °C).[118] Reprinted with permission from Elsevier B.V., copyright 2021.

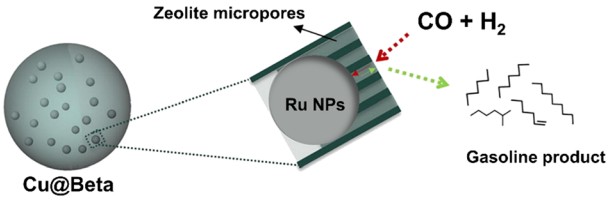

Fig. 15 The direct synthesis of the gasoline product from CO hydrogenation using the Ru@NaY catalyst.[121] Reprinted with permission from Elsevier B. V., copyright 2021.

hydrogenation. Xiao *et al.*[119] also found during CO_2 hydrogenation that Rh@HZSM-5 was more likely to generate methane with a selectivity of 98.2%, while the Rh@S-1 catalyst was more likely to generate CO with a selectivity of 79.8% under the same conditions. The different results could be mainly attributed to the fact that HZSM-5 favored hydrogen spillover for the further deep hydrogenation of CO to methane.

5.2 Selectivity

5.2.1 Na-type zeolite. With the aid of "shape-selective catalysis" of zeolite, zeolite-encapsulated metal catalysts can show unique selectivity compared to traditional metal catalysts without confinement. Fisher–Tropsch (F–T) synthesis product is characteristic of Anderson–Schulz–Flory (ASF) distribution, and a broad distribution with selectivities for C_2–C_4, gasoline (C_5–C_{11}), and diesel (C_{12}–C_{20}) are limited to 58%, 48%, and 40%, respectively.[120] Xiao *et al.*[121] proposed a new strategy to tune the product selectivity in F–T synthesis, and the selectivity of the resulting gasoline product could overcome the limitations of the ASF (Fig. 15). The gasoline selectivity of the prepared Ru@NaY catalyst (Ru particles encapsulated in NaY zeolite) was 64.3%, which was about 2 times higher than that (32.8%) of Ru/NaY (Ru particles were located on the outer surface of the Y zeolite). This is owing to the encapsulation of Ru particles within the FAU zeolite crystals, where the 12-MR zeolite aperture could inhibit the C–C coupling reaction of olefins to long-chain hydrocarbons and improve the selectivity of the gasoline product. Xing *et al.*[122] prepared the Pt@Y catalyst by encaging Pt nanoparticles in Y zeolite and for the hydrogenation of aromatic ketones. Due to the restricted adsorption conformation of aromatic ketones by the micropores of the Y zeolite, the Pt@Y catalyst exhibited 100% selectivity of aromatic alcohols even at conversion ~100%.

5.2.2 H-type zeolite. The product distribution in a tandem catalytic reaction can be manipulated by tailoring the proximity between the acid and metal sites in zeolite-supported metal catalysts.[123,124] In the biomass upgrading process, several consecutive steps are often required to be converted into the desired products. However, not all catalytic materials with different active sites could guide the tandem reaction with steps in the desired sequence. Xu *et al.*[27] designed the Pt@H-ZSM-5 catalyst *via* a cationic polymer-assisted synthesis and demonstrated the molecular level proximity between Brønsted (B) acid and Pt sites. As shown in Fig. 16, in the reaction of furfural converted to VA and EV, Pt@H-ZSM-5 and Pt/H-ZSM-5 (obtained by incipient wetness impregnation) showed different reaction pathways; the yield of the target product was 86% and 5%, respectively. The high selectivity on the Pt@H-ZSM-5 catalyst was attributed to the distribution of metal and acid sites, which could change the steps of the tandem reaction. Recently, they used a similar method to synthesize the Pt@H-BEA catalyst, which could efficiently convert cyclopentanone to dicyclopentane and decalin in a tandem reaction with a yield of 78%.[109]

5.3 Stability

Supported metal catalysts would be deactivated under harsh reaction conditions due to sintering, leaching, carbon deposition, or poisoning of metal active centers (Fig. 17). Zeolites have a rigid framework and high thermal and hydrothermal stability. Besides, the pores of the zeolite can keep the encapsulated metal species isolated from each other, reducing the aggregation and sintering of metal species. Therefore, encapsulating metal species into zeolites is an effective strategy to improve their stability.

5.3.1 Sintering- and leaching-resistant stability. Metal leaching and sintering are inherent properties of supported metal catalysts, which would lead to catalyst deactivation during catalytic reactions. Wang *et al.*[125] encapsulated Pd

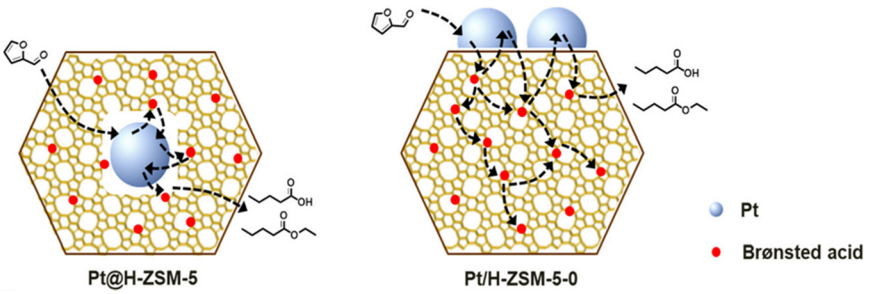

Fig. 16 The conversion of furfural into VA/EV over Pt@H-ZSM-5 and Pt/H-ZSM-5.[27] Reprinted with permission from American Chemical Society, copyright 2020.

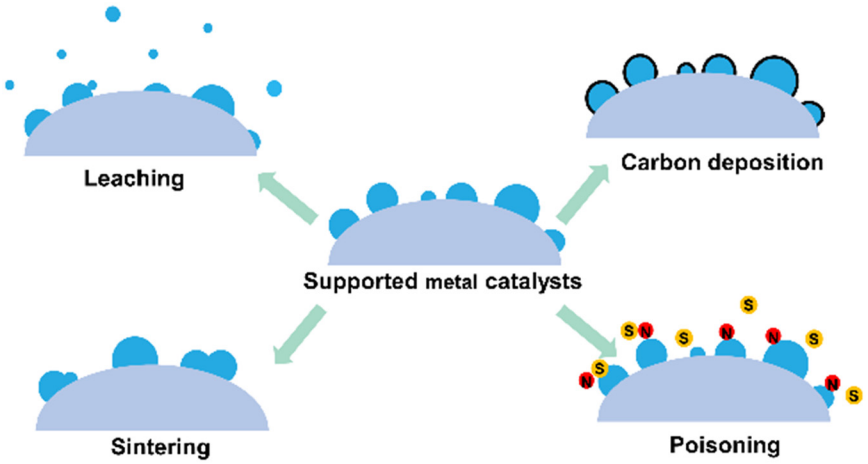

Fig. 17 Schematic of supported metal catalysts deactivation modes.

particles within zeolite Y (Pd@Y) to improve their antisintering ability under harsh reaction conditions. The resultant catalyst was stable even after calcining at 800 °C, while the catalyst synthesized by the traditional deposition method (Pd/Y) sintered significantly after the same calcination treatment. In addition, the Pd@Y catalyst also exhibited high stability and regeneration performance in CO oxidation reaction. The TEM images showed that the Pd size in Pd@Y changed negligibly after CO oxidation reaction, but the Pd size of Pd/Y increased from 3.7 to 19.9 nm. Pt particles encapsulated in the traps were produced by the dealumination of the Y zeolite, hindering the movement of Pd nanoparticles and improving the stability of Pt@Y. Zhang *et al.*[126] prepared Pd@Beta catalyst by encapsulating Pd particles (~1.6 nm) within Beta zeolite. During the synthesis, Pd/Beta synthesized by the wet-impregnation approach was used as a seed and then crystallized in aluminosilicate gels. The Pd@Beta catalyst exhibited extremely high thermal and hydrothermal stability, and the size of Pd particles was almost unchanged even at 600 °C for 240 min in air. Moreover, the Pt@Beta catalyst also showed remarkable stability in water-gas shift (WGS) reaction. As shown in Fig. 18, the Pt@Beta catalyst remained highly active after the reaction for 6000 min, while the conventional Pt/Beta showed low catalytic activity after the reaction for 2640 min. Simultaneously, the TEM images showed that the size of Pt particles in the used Pt@Beta still retained the original diameter range of 0.8–3.2 nm. A similar procedure was also applied to synthesize Rh@Beta, Rh@MOR, Ag@Beta, Pt@MOR, Ag@MOR, and Pd@S-1, and the resultant catalysts all exhibited high thermal and hydrothermal stability.[124] For the leaching-resistant stability via encapsulation, Liu *et al.*[70] confined Au clusters in MCM-22 zeolite using 2D-to-3D zeolite transformation strategy (Au@MCM-22). The as-encapsulated Au clusters in zeolite were protected from leaching into the reactant during the liquid-phase oxidation of cyclohexane to cyclohexanol and cyclohexanone.

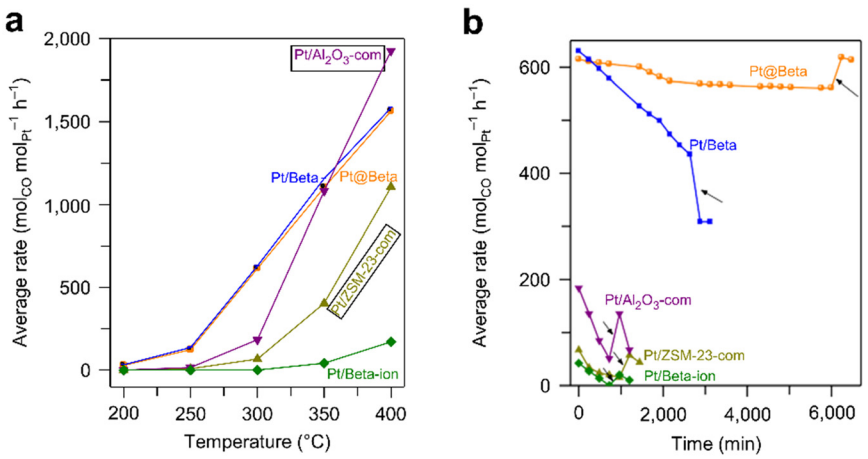

Fig. 18 Average rates of various catalysts in the WGS reaction as a function of (a) temperature and (b) time (reaction conditions: 20 mL min^{-1} of reactant gas (7% CH_4 + 3.3% O_2 + 79.7% He), GHSV = 480 000 mL g_{Pd}^{-1} h^{-1}, 600 °C).[126] Reprinted with permission from Spring Nature, copyright 2018.

The dry reforming of methane (DRM) is an environment-friendly reaction that can convert methane and carbon dioxide into hydrogen and carbon monoxide.[127–129] Ni-based catalysts are the most commonly used catalysts for the DRM reaction, but they usually tend to sinter at high reaction temperature. Several works have proved that fixing Ni clusters in zeolites can effectively improve their stability *via* the restriction of the zeolite framework.[130,131] Dai *et al.*[132] conducted further studies on DRM catalysts and found that the simultaneous encapsulation of Pt and Ni in S-1 zeolite could exhibit excellent stability and anticoking properties. The excellent stability of Ni-Pt@S-1 could be attributed to the interaction between Ni and Pt, which could suppress the sintering of Ni and keep the metal particles highly dispersed. Next, Dai *et al.*[28] synthesized the Fe_2O_3–CuO@S-1 catalyst to catalyze phenol degradation. The obtained bimetallic catalyst exhibited higher dispersion and smaller size than Fe_2O_3@S-1 and CuO@S-1. For phenol degradation, Fe_2O_3–CuO@S-1 showed superior activity and resistance to sintering.

5.3.2 Anti-carbon deposition stability. Carbon deposition can cover the active sites and block zeolite pores, resulting in a drastic decrease in the surface area and pore volume, which may exacerbate mass transfer limitations and lead to catalyst deactivation. Encapsulating metal species into zeolites is a promising strategy to effectively prevent carbon deposition in high-temperature catalytic reactions. Ismaila *et al.*[133] prepared the Ni@S-1 catalyst *via* one-pot hydrothermal synthesis for the catalytic steam reforming of glycerol (SRG) reaction. As a comparison, the Ni/S-1 catalyst was synthesized by a conventional impregnation method. The Ni@S-1 catalyst exhibited high activity in SRG reaction at 750 °C with glycerol conversion of ~99% and hydrogen yield of ~60%, while the Ni/S-1 catalyst showed a comparatively low glycerol conversion of 73% and hydrogen yield of 45%. The activity of the Ni/S-1 catalyst kept decreasing gradually as a function of TOS (time on stream), while Ni@S-1 maintained similar activity to the initial activity after 100 h of reaction. In the thermogravimetric analysis (TGA), the weight loss of used Ni/S-1 was ~15% higher than that of used Ni@S-1 (~8%), demonstrating the anticoking ability of Ni@S-1. Significantly, the introduction of mesopores *via* post-synthetic TPAOH treatment could further improve the activity and anticoking ability of Ni@S-1. In the SRG reaction, the obtained Ni@HolSi-1 catalyst showed about 99% glycerol conversion and about 70% H_2 yield after reacting at 750 °C for 100 h. In the TGA test, the weight loss of used Ni@HolSi-1 was less than 0.5%.

5.3.3 Anti-poisoning stability. Poisoning is a result of strongly chemisorbed species present in the reaction system, which include reactants or impurities such as N, S, or P-containing species. Metal poisoning usually occurs to cause deactivation. The confinement of metal species within zeolites can prevent the poisoning of active sites by large organosulfur species. Iglesia *et al.*[134] encapsulated Pt and Rh clusters within NaA zeolite using MPS as ligands. NaA micropore aperture is 0.41 nm smaller than that of thiophene (0.46 nm), preventing thiophene from contacting the encapsulated metal clusters. During ethene hydrogenation, the hydrogenation rates of Pt and Rh clusters in NaA decreased by only ~20% with the addition of thiophene, while the SiO_2-supported samples showed no hydrogenation activity with thiophene introduction.

The poisoning of Pd is a general problem for many supported Pd nanoparticle catalysts, which is also a serious problem faced by Pd catalyst industries. In the hydrogenation of phenylacetylene to styrene, the TOF values over the commercial Pd/C and Pt/Y catalysts decreased by 91.7% and 85.7% with the *in situ* addition of thiophene, respectively.[135] Very interestingly, encaging single Pt atoms in SOD cages within the Y zeolite exhibited high catalytic activity with only a 12.5% reduction in TOF value under the equivalent reaction condition. This antipoisoning stability could be attributed to the confinement effect of zeolite voids, which could prevent metal species from contacting with toxic substances in the reaction medium. In addition, the zeolite framework could interact strongly with metals due to the confinement effect, resulting in partial charge transfer from Pt to skeleton oxygen and weaken the interaction of encaged $Pt^{\delta+}$ with poisons.

6 Catalysis of confined catalysts

In this section, we discuss the catalytic properties of zeolite-encapsulated metal catalysts in some important catalytic reactions. The properties of representative zeolite-encapsulated metal catalysts and their catalytic applications are summarized in Table 2.

6.1 Application in traditional chemical industry

6.1.1 Dehydrogenation of propane. Propylene is one of the most important industrial raw materials and is mainly produced through two major processes, namely, catalytic cracking and naphtha cracking. Due to the scarcity of fossil fuels and the discovery of shale gas, PDH has received extensive attention and is considered as a promising approach to meet the ever-increasing demand for propylene. Supported Pt-based catalysts are widely used in the PDH process. Liu *et al.*[57] confined Pt species into purely siliceous MCM-22 zeolite by 2D-to-3D zeolite transformation method using dimethylformamide (DMF) as a reductant and capping agent. HAADF-HRSTEM measurements revealed that Pt species are located in the surface cups, cavities, and 12-MR supercages of MCM-22 zeolite in the form of single atoms and small clusters. The Pt/MCM-22-imp catalyst prepared by the impregnation method had a larger metal size ranging from 1 to 5 nm. The resulting Pt@MCM-22 and Pt/MCM-22-imp were used in the PDH reaction. Pt@MCM-22 established high propane dehydrogenation activity, and the reaction rate was about 5 times higher than that of Pt/MCM-22-imp. Pt@MCM-22 had excellent stability; after five regeneration cycles at 550 °C, the activity of the Pt@MCM-22 catalyst was still 90% of the initial activity, while the activity of Pt/MCM-22-imp was less than 60% of the initial activity. Adding secondary metal elements (*e.g.*, Sn,[42,86,137] Zn,[37,136,151,152] Fe,[153] and Cu (ref. 138)) to Pt-based catalysts can change the

Table 2 Summary of properties of various zeolite-encapsulated metal catalysts and the corresponding catalytic activity for some important catalytic reactions

Catalyst	Metal particle size (nm)	Metal loading (wt%)	Reaction condition	Catalytic results	Ref.
PDH reaction					
Pt@MCM-22	~1	0.11	T = 550 °C; WHSV = 3.2 h^{-1}; C_3H_8/N_2 = 30/3 mL min^{-1}	C_3H_6 formation rate = 2.21 $mol_{C_3H_6}$ g_{Pt}^{-1} h^{-1}	57
PtZn@S-1	<1	0.23	T = 550 °C; WHSV = 6.5 h^{-1}; C_3H_8/N_2 = 11/19 mL min^{-1}; 60 h	C_3H_6 formation rate = 28.2 $mol_{C_3H_6}$ g_{Pt}^{-1} h^{-1}; $Con_{C_3H_8}$ = 45.3–42.0%; $Sel_{C_3H_6}$ = 99–99.9%; K_d = 0.002 h^{-1}	136
K–PtSn@MFI	~0.55	0.40	T = 600 °C; WHSV = 29.5 h^{-1}; C_3H_8/N_2 = 5/16 mL min^{-1}; 25 h	C_3H_6 formation rate = 66.26 $mol_{C_3H_6}$ g_{Pt}^{-1} h^{-1}; $Con_{C_3H_8}$ = 38.7–31.9%; $Sel_{C_3H_6}$ = 97–97.5%; K_d = 0.012 h^{-1}	137
PtCu@S-1	~2.0	0.1	T = 610 °C; WHSV = 1.3 h^{-1}; 3 h	C_3H_6 formation rate = 12.95 $mol_{C_3H_6}$ g_{Pt}^{-1} h^{-1}; $Con_{C_3H_8}$ = 46.0–9.0%; $Sel_{C_3H_6}$ = 93.2–91.0%; K_d = 0.7 h^{-1}	138
GaPt@S-1	<1	0.092	T = 600 °C; WHSV = 0.65 h^{-1}; C_3H_8/N_2 = 1/19 mL min^{-1}; 24 h	C_3H_6 formation rate = 20.5 $mol_{C_3H_6}$ g_{Pt}^{-1} h^{-1}; $Con_{C_3H_8}$ = 45.9–41.6%; $Sel_{C_3H_6}$ = 92.0–95.0%; K_d = 0.068 h^{-1}	139
PtLa/mz-deGa	~3	1.0	T = 580 °C; WHSV = 11.0 h^{-1}; C_3H_8 = 4.6 mL min^{-1}; 720 h	C_3H_6 formation rate = 10.05 $mol_{C_3H_6}$ g_{Pt}^{-1} h^{-1}; $Con_{C_3H_8}$ = 40.0–8.0%; $Sel_{C_3H_6}$ = 95.0–96.0%; K_d = 0.003 h^{-1}	38
CO hydrogenation					
Co@S1	—	10	T = 260 °C; P = 1.0 MPa; H_2/CO = 2; W/F = 6 g h mol^{-1}	Con_{CO} = 45.8%; $Sel_{gasoline}$ = 68.8%	140
RhMn@S-1	~2.7	Rh (0.76) Mn (0.85)	T = 320 °C; P = 1.5 MPa; H_2/CO = 2; F = 30 mL min^{-1}	Con_{CO} = 42.4%; [a]$Sel_{C_2\text{-}oxy}$ = 88.3%	141
Fe@NaY	~2.13	5.9	T = 300 °C; P = 3 MPa; H_2/CO = 2; F = 20 mL min^{-1}	Con_{CO} = 91.2%; $Sel_{C_2^=-C_4^=}$ = 36.2%	142
CO_2 hydrogenation					
Rh@S-1	~4.3	0.45	T = 500 °C; P = 1.0 MPa; $H_2/CO_2/Ar$ = 3/1/1; F = 30 mL min^{-1}	Con_{CO_2} = 51.6%; Sel_{CO} = 79.8%	119
Rh@HZSM-5	~5.0	0.42	T = 500 °C; P = 1.0 MPa; $H_2/CO_2/Ar$ = 3/1/1; F = 30 mL min^{-1}	Con_{CO_2} = 68.2%; Sel_{CH_4} = 98.2%	119
Na–Rh@S-1	2.4–2.6	0.73	T = 250 °C; P = 5 MPa; H_2/CO_2 = 4; F = 15 mL min^{-1}	Con_{CO_2} > 10%; $Sel_{ethanol}$ = 24%	143
Furfural hydrogenation					
Pd@Na-ZSM-5	5–10	0.89	T = 150 °C; P_{H_2} = 1 MPa; 0.077 g furfural (FFL); 5 mL isopropanol as solvent; 12 h	Con_{FFL} = 76%; Sel_{FAL} = 74%	144
Cu@TS-1	~1.9	2.14	T = 110 °C; P_{H_2} = 1 MPa; 0.3 FFL; 23.56 g isopropanol as solvent; 2 h	Con_{FFL} = 45.9%; Sel_{FAL} = 74.7%	109
Na–Cu@TS-1	~1.8	2.05	T = 110 °C; P_{H_2} = 1 MPa; 0.3 g FFL; 23.56 g isopropanol as solvent; 2 h	Con_{FFL} = 93.0%; Sel_{FAL} = 98.1%	109
The conversion of 5-hydroxymethylfurfural (HMF)					
Pt@Y	~1.9	1.23	T = 80 °C; P_{H_2} = 2 MPa; 12.7 mg HMF; 1.5 mL H_2O; 4 h	Con_{HMF} = 100%; Sel_{BHMF} > 99%	145
Pt@Beta	~1.61	0.20	T = 90 °C; P_{H_2} = 2 MPa; 12.6 mg HMF; $n_{Na_2CO_3}/n_{HMF}$ = 6; 4 mL H_2O; 24 h	Con_{HMF} = 99%; Sel_{FDCA} = 98%	146
Hydrogen generation					
Rh@NaY	—	1.2	T = 25 °C; 10 mL 100 mM ammonia borane (AB); n_{Rh}/n_{AB} = 0.002	[b]TOF = 92 min^{-1}; E_a = 66.9 kJ mol^{-1}	147
Rh@S-1-C	—	0.28	T = 25 °C; 1 mL 1 M AB; n_{Rh}/n_{AB} = 0.0011	[b]TOF = 195 min^{-1}	36
Rh@S-1-H	Single atom	0.28	T = 25 °C; 1 mL 1 M AB; n_{Rh}/n_{AB} = 0.0011	[b]TOF = 432 min^{-1}; E_a = 75.5 kJ mol^{-1}	77

Table 2 *(continued)*

Catalyst	Metal particle size (nm)	Metal loading (wt%)	Reaction condition	Catalytic results	Ref.
$Rh_{0.8}Ru_{0.2}$/SP-S-1	~0.78	Rh (0.36) Ru (0.08)	T = 25 °C; 1 mL 1 M AB; n_{metal}/n_{AB} = 0.001	[b]TOF = 620 min^{-1}; E_a = 75.5 kJ mol^{-1}	148
$Rh_{0.8}Ru_{0.2}$/SP-ZSM-5	~0.70	Rh (0.36) Ru (0.08)	T = 25 °C; 1 mL 1 M AB; n_{metal}/n_{AB} = 0.001	[b]TOF = 1006 min^{-1}; E_a = 56.5 kJ mol^{-1}	148
Pd@S-2	~1.5	0.41	T = 50 °C; 5 mL 1 M formic acid (FA); n_{Pd}/n_{FA} = 0.005	[c]TOF = 3349 h^{-1}; E_a = 30.3 kJ mol^{-1}	149
$PdMn_{0.6}$@S-1	~1.0	Pd (0.59) Mn (0.16)	T = 60 °C; 1.5 mL 2 M FA; n_{Pd}/n_{FA} = 0.012	[d]TOF = 6860 h^{-1}; E_a = 56.5 kJ mol^{-1}	150

[a] Selectivity of ethanol in total oxygenates. [b] TOF is the total turnover frequency when the conversion of AB reaches 100%. [c] TOF value calculated for the complete time of gas release. [d] TOF value calculated for the complete time of gas release and Pd metal atoms.

electron density of Pt atoms, thereby affecting the catalytic performance of Pt-based catalysts. For instance, Wang *et al.*[136] encapsulated bimetallic PtZn nanoclusters inside S-1 zeolite using Pt-ethylenediamine and Zn-ethylenediamine complexes as precursors *via* direct hydrothermal crystallization. TEM images indicated that the PtZn bimetals in 0.3Pt0.5Zn@S-1 were homogeneously dispersed in S-1 zeolite in the form of ultrasmall-sized nanoclusters, while the PtZn bimetals had a larger size (~6.1 nm) in 0.3Pt0.5Zn/S-1 (prepared by the impregnation method). Introducing Zn into Pt species could significantly improve the PDH performance. As shown in Fig. 19a, the 0.3Pt0.5Zn@S-1 catalyst exhibited super high propylene selectivity up to 99%, and the TOF value was 74.7 min^{-1} at 450 °C. In addition, the 0.3Pt0.5Zn@S-1 catalyst showed outstanding stability due to the confinement effect of zeolites. After 60 h of reaction, the deactivation of 0.3Pt0.5Zn@S-1 was not obvious, and the deactivation rate was 0.002 h^{-1}, 7.5 times lower than that over 0.3Pt0.5Zn/S-1 (Fig. 19b). Moreover, the 0.3Pt0.5Zn@S-1 catalyst established the recycling stability of PDH. As shown in Fig. 19c, the activity obtained over the catalyst was almost the same as that of the fresh catalyst during four cycles after a simple oxidation–reduction process.

Besides the introduction of transitional metal, rare-earth metals is also included to improve the performance of Pt-based catalysts for the PDH reaction. Ryoo *et al.*[38] prepared Pt–La alloy nanoparticles incorporated in the mesoporous MFI zeolite (PtLa/mz-deGa). Mesoporous Ga-MFI zeolite was treated by HNO_3 to remove framework Ga atoms, and then Pt and La were introduced by the impregnation method, followed by treatment under O_2 flow at 350 °C and subsequently under H_2 at 700 °C. The addition of La significantly enhanced the catalytic activity, selectivity, and durability of the catalyst in the PDH reaction. The PtLa/mz-deGa catalyst exhibited a high of 40% propane conversion at the initial stage and 8% propane conversion after 30 days on stream, while the conventional $PtSn/Al_2O_3$ catalyst deactivated in 1 day. The silanol nests in zeolites could promote the generation of atomically-dispersed La, which were much easier to diffuse onto Pt to form the alloy. Apart from La, Y and Ce were also added into Pt-based catalysts and showed outstanding catalytic activity for PDH.[38]

6.1.2 The conversion of CO and CO_2

6.1.2.1 CO hydrogenation. The catalytic transformation of syngas (a mixture of H_2 and CO) that is obtained from biomass, coal, natural gas, and carbon-based waste, has become a sustainable option to produce valuable products (*e.g.*, light olefins, aromatics, and liquid fuels).[154–157] The zeolite-encapsulated metal catalysts are used as efficient catalysts for the hydrogenation of CO. Javed *et al.*[140] reported the preparation of embedded Co nanoparticles within S-1 zeolite (Co@S1) by a solvent-free method. For the hydrogenation of CO reaction, the Co@S1 catalyst exhibited a superhigh selectivity of gasoline up to ~70%, while the relatively lower selectivity of gasoline (~48%) was observed in Co/S1 synthesized by impregnation. The large differences in

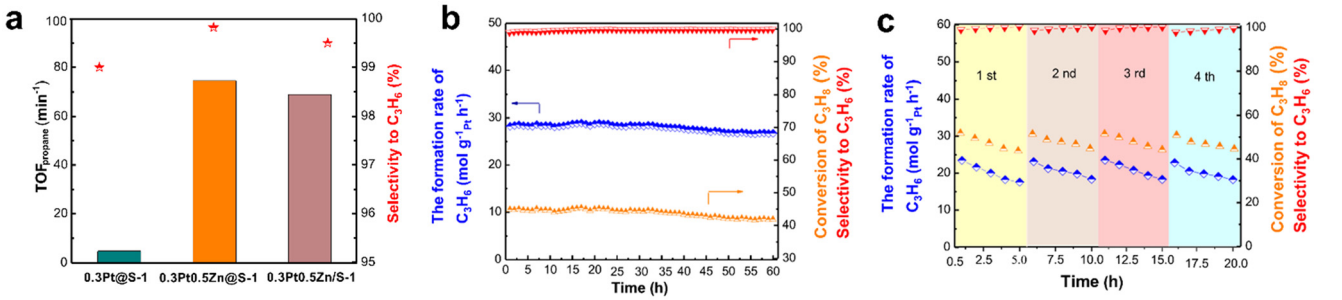

Fig. 19 (a) The TOF of Pt-based catalysts at 450 °C; (b) stability testing over 0.3Pt0.5Zn@S-1 at 550 °C for 60 h; (c) recyclability of 0.3Pt0.5Zn@S-1 in the PDH reaction at 600 °C (reaction conditions: 200 mg catalysts, atmospheric pressure, $WHSV_{propane}$ = 6.5 h^{-1}, and $C_3H_8:N_2$ = 11:19 with flow rate 30 mL min^{-1}).[136] Reprinted with permission from Elsevier Inc., copyright 2020.

the catalytic selectivity could be attributed to the unique zeolite microporous structure, which could suppress C–C coupling to produce long-chain hydrocarbons. In addition, the direct transformation of syngas into oxygenated chemicals, with high selectivity, also attracted extensive attention from researchers. For example, Xiao *et al.*[141] fixed RhMn nanoparticles within S-1 zeolite by a solvent-free crystallization strategy using the metal-containing zeolite as seeds. The newly-formed zeolite covered on the seed, fixing them within zeolite crystals as a core–shell structure. According to tomographic TEM and STEM images, RhMn nanoparticles with an average size of ~2.7 nm were mostly fixed within the S-1 zeolite (RhMn@S-1), while most RhMn nanoparticles with an average size of ~3.2 nm were on the external surface of the S-1 zeolite in the supported Rh catalyst (RhMn/S-1). The RhMn@S-1 catalyst showed excellent C_2-oxy productivity, giving C_2-oxy productivity at 105.0 mol mol_{Rh}^{-1} h^{-1}, which was nearly 3 and 9 times higher than that over RhMn/S-1 (42.3 mol mol_{Rh}^{-1} h^{-1}) and RhMn/Al_2O_3 (11.7 mol mol_{Rh}^{-1} h^{-1}). The unusual catalytic performances of RhMn@S-1 originated from zeolite fixation and Mn–O–$Rh^{\delta+}$ structure, which could enhance the C–C coupling reaction to produce C_2-oxy. Moreover, the rigid zeolite sheath could inhibit Rh sintering and stabilize the active Mn–O–$Rh^{\delta+}$ structure, which is beneficial to improve the stability.

6.1.2.2 CO_2 hydrogenation. In recent years, the hydrogenation of CO_2 into useful chemicals (*e.g.*, CO,[158] methane,[159] olefin,[160] gasoline,[161] and alcohol[143]) has attracted extensive attention due to its great potential in the recycling economy and sustainable development. Metal@zeolite catalysts have been used for CO_2 hydrogenation and showed superior catalytic activity. For example, Ni nanoparticles confined in the ZSM-5 zeolite (Ni@recryst-ZSM-5) exhibited a high CH_4 selectivity, high conversion, and excellent durability in CO_2 hydrogenation.[47] Ni@recryst-ZSM-5 resulted in 49% conversion of CO_2 and 93% selectivity of CH_4, which was significantly higher than that of Ni/*meso*-ZSM-5 (44% conversion and 84% selectivity) prepared by the impregnation method. Moreover, the initial CO_2 conversion and CH_4 selectivity of Ni@recryst-ZSM-5 did not decrease after 50 h at 450 °C. CO_2 could also be transformed into ethanol over metal@zeolite catalysts. For instance, Zhang *et al.*[143] presented a study on the application of Rh nanoparticles confined within the S-1 zeolite (Rh@S-1) *via* the ligand-protected hydrothermal crystallization method. The Na-modified Rh@S-1 (Na-Rh@S-1) was also prepared by a similar procedure to those of Rh@S-1 using ethylenediaminetetraacetic acid (EDTA) as the ligand in the presence of Na^+. According to tomographic TEM images, the mean sizes of Rh particles in Rh@S-1 and Na–Rh@S-1 were in the range of 2.4–2.6 nm, while the mean sizes of Rh particles in Na–Rh/S-1 prepared by impregnation was ~4.2 nm. In the CO_2 hydrogenation reaction, Rh@S-1 showed a CO_2 conversion of 2.9% and a negligible amount of ethanol in products, and the Na–Rh@S-1 catalyst exhibited enhanced ethanol selectivity (~24%) and CO_2 conversion (>10%). More importantly, the high catalytic activity of Na–Rh@S-1 can be maintained after 100 h reaction without obvious deactivation, and the mean size of Rh nanoparticles remained unchanged. However, Na–Rh/S-1 suffered from a fast deactivation in 50 h of reaction, and the mean size of Rh nanoparticles increased significantly from 4.2 to 7.8 nm. The specific encapsulated structure stabilized and protected the active Rh nanoparticles against metal sintering, and the presence of Na^+ induced the coexistence of Rh^0 and Rh^+ species, resulting in the increased selectivity of ethanol.

For the conversion of CO and CO_2 *via* hydrogenation, selectivity is proven to be sensitive to the microporous environment of zeolites as the tandem conversion of CO_x to hydrocarbons requires metal and acid sites. Xiao *et al.*[119] confined Rh nanoparticles within a series of MFI-type zeolite (HZSM-5 and S-1) for the hydrogenation of CO_2. The as-prepared Rh@S-1 catalyst showed a high selectivity to CO (79.8%) with 51.6% conversion of CO_2 at 500 °C. When changing the S-1 support to HZSM-5 (Rh@HZSM-5), the methane selectivity was significantly improved, giving a CH_4 selectivity of 98.2% at CO_2 conversion of 68.2% at 500 °C. This stems from the fact that the Rh@S-1 zeolite had low hydrogenation activity and fast desorption of CO to minimize further deep hydrogenation, while Rh@HZSM-5 featured with enhanced CO adsorption property and strong hydrogen spillover could further hydrogenate CO to obtain CH_4. In addition, the synergistic effect of acidic sites and metal sites in metal@zeolite catalysts can be utilized to increase the efficiency of producing a specific range of hydrocarbons.[162] For instance, Khodakov *et al.*[163] encapsulated Ru nanoparticles into the zeolite by coating the ZSM-5 zeolite containing Ru metals with a shell MFI-type material (ZSM-5/Ru/ZSM-5). The ZSM-5/Ru/ZSM-5 catalyst showed the highest selectivity toward iso-paraffins in F–T synthesis. Paraffins and olefins were formed simultaneously on Ru active sites, and then the subsequent isomerization of these intermediates requires the presence of both Ru and acid sites; thus, the close proximity between Ru metals and acidic sites facilitated the production of iso-paraffins.

Apart from propane dehydrogenation and the conversion of CO and CO_2, zeolite-encapsulated metal catalysts have also been employed to catalyze other reactions, such as methane oxidation,[164] hydrogenation of alkenes and alkynes,[165,166] alkene epoxidation,[167] and aromatics hydrogenation.[168]

6.2 Application in biomass conversion

At present, with the continuous consumption of fossil resources such as coal, oil, and natural gas in the world, the development and utilization of biomass energy has attracted more and more attention. Biomass is all organic matter that is directly or indirectly utilized by green plants photosynthesis. Converting biomass-derived platform compounds (*e.g.*, furfural, lignin, and 5-hydroxymethylfurfural) into value-added chemicals is an efficient way to utilize biomass resources and can bring huge economic benefits. The zeolite-encapsulated metal catalysts are

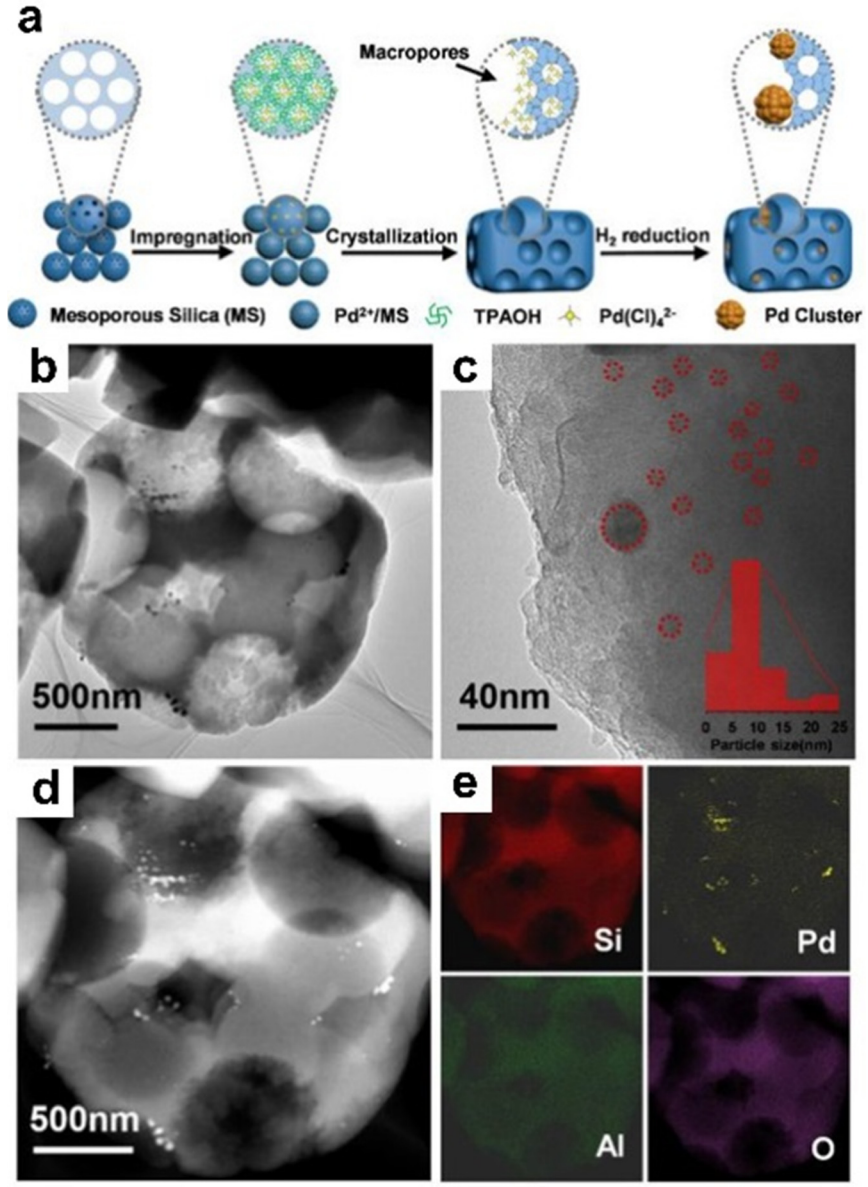

Fig. 20 (a) Synthesis of Pd@ZSM-5; (b and c) TEM images of Pd@ZSM-5; (d) HAADF-STEM image of Pd@ZSM-5, and (e) the corresponding EDS mapping images for Si, Al, Pd, and O elements.[144] Reprinted with permission from Wiley-VCH, copyright 2020.

an effective catalyst for the conversion of biomass-derived platform compounds and show high activity and production selectivity.

For instance, Liu *et al.*[144] reported a steam-thermal approach for the preparation of Pd nanoparticles confined in ZSM-5 zeolite. The synthesis process is shown in Fig. 20a. TEM measurements demonstrated that the Pd particle size in Pd@ZSM-5 was 5–10 nm and dispersed throughout ZSM-5 crystals (Fig. 20b–e). The Pd@Na-ZSM-5 (ion exchange of Pd@ZSM-5 with Na^+ to decrease the amount of Brønsted acid sites (BAS)) catalyst exhibited superhigh selectivity for furfuryl alcohol up to 74%, while that of Pd/Na-ZSM-5 was only 10%. Significantly, the Pd@Na-ZSM-5 catalyst also exhibited excellent hydrothermal stability and steam stability. After Pd@Na-ZSM-5 was exposed to water at 110 °C and steamed for 3 days, the structure and microporosity did not change significantly. Recently, Cao *et al.*[109] encapsulated Cu nanoparticles within TS-1 zeolite (Cu@TS-1), which showed a satisfactory catalytic property in the selective hydrogenation of furfural into furfuryl alcohol. In addition, Na–Cu@TS-1 was synthesized by the Na ion-exchange process of Cu@TS-1. According to the HAADF-STEM images, uniform Cu nanoparticles with a mean size of ~1.9 nm and ~1.8 nm were highly dispersed in Cu@TS-1 and Na–Cu@TS-1, respectively. N_2O chemisorption results further proved that Na–Cu@TS-1 had a slightly higher Cu dispersion (65.6%) than Cu@TS-1 (62.7%). Moreover, Na–Cu@TS-1 showed a high furfural conversion of 93% and furfuryl alcohol selectivity of 98.1%, while Cu@TS-1 exhibited low furfural conversion of 45% and furfuryl alcohol selectivity of 74.7%

under the same reaction conditions. In the recycling tests, Na–Cu@TS-1 also showed a drop in the activity (furfural conversion from initial 95.0 to 32.2% and furfuryl alcohol yield from initial 93.8 to 30.4%) after four consecutive runs, and the catalytic performance could be fully restored by Na re-addition regeneration (85.5% furfural conversion and 83.7% furfuryl alcohol yield). The outstanding performance of Na–Cu@TS-1 originated from the modulation of the zeolite microenvironment by Na^+ and the spatial restriction from the TS-1 framework.

HMF is a well-known biomass-based platform compound and can be used to prepare a variety of fine chemicals, polymer precursors, and liquid fuels. For example, HMF can be converted to 2,5-bis-(hydroxymethyl)-furan (BHMF), 2,5-dimethylfuran (DFM) or C_6 alkane, and other chemicals by hydrodeoxygenation. Chen *et al.*[145] synthesized the Pt@Y catalyst by one-pot hydrothermal synthesis method using $[Pt(NH_3)_4](NO_3)_2$ as metal precursors. HRTEM measurements demonstrated that the Pt nanoparticles were highly dispersed in Y zeolite crystals. The HAADF-STEM image further suggested that the Pt particles were uniformly distributed throughout the Y zeolite, and the average size was ~1.9 nm. In the hydrogenation of HMF, the Pt@Y catalyst exhibited nearly 100% catalytic selectivity of BHMF, while Pt/Y only gave 10% catalytic selectivity to BHMF at the same conversion of 90%. After four cycles, Pt@Y also maintained the catalytic activity and selectivity to the original without an obvious aggregation or coalescence of Pt particles.

The conversion of biomass-derived feedstocks to value-added products typically requires a number of sequential catalytic steps and as a result, a catalyst that provides offers activity in these different reactions. Therefore, the rational combination of metal and acid sites is crucial in catalyst design. Encapsulating metal sites into acidic formed zeolite, the close proximity between metal and acid sites can provide additional benefits and sometimes synergistic effects in catalysis. For example, the Cu@HZSM-5 catalyst was synthesized *via* an *in situ* hydrothermal synthesis method.[169] As a result, the Cu@HZSM-5 catalyst with close proximity between metal and acid sites showed a high yield of 68.1% VA in the direct conversion of γ-valerolactone, while the Cu/HZSM-5 with metal sites on the external surface of zeolite showed only a VA yield of 34.8% at the same reaction conditions. Density functional theory (DFT) calculations confirmed that Cu clusters near the acid sites in the zeolite significantly changed the C–O bond activation route, thereby changing the reaction pathway to increase the yield of VA. Meanwhile, the stability of Cu@HZSM-5 was also enhanced with less coking. Moreover, Cho *et al.*[26] also demonstrated a synergistic effect in Pt@HZSM-5 for tandem aldol condensation and hydrogenation of furfural and acetone to produce hydrogenated C_8. Well-dispersed Pt nanoparticles in the MFI zeolite with an average particle size of 5.4 nm were obtained *via* the dry-gel synthesis method. The results of model reactions with different sizes substrates demonstrated 90% encapsulation fraction of Pt nanoparticles within the zeolite matrix. In this case, the entire cascade reactions can be processed inside the pores of the MFI zeolite. The Pt located in the zeolite could more efficiently affect the tandem reactions, and the Pt@HZSM-5 catalyst showed a high yield of 87% C_8-hydrogenated, while Pt/HZSM-5 (Pt metal located on the external surface of the zeolite) favored the conversion of furfural *via* metal-mediated hydrogenation, hydrodeoxygenation, and decarbonylation and showed only a VA yield of 24%.

Zeolite-encapsulated metal catalysts have also been employed to convert other biomass-based platform compounds into target chemicals, such as 5-hydroxymethylfurfural to 2,5-furandicarboxylic (FDCA) over the Pd@Beta catalyst,[146] furfuryl alcohol to tetrahydrofurfuryl alcohol over Pd–Si–ZSM-22,[170] cyclopentanone to bicyclopentane and decalin over Pt@H-BEA,[110] and the hydrodeoxygenation of guaiacol to produce cyclohexane over Ru@HMCM-22.[171]

6.3 Application in hydrogen generation

Hydrogen has emerged as a promising energy replacement to meet the ever-increasing energy challenges. In recent years, liquid-phase hydrogen storage materials (*e.g.*, ammonia borane and formic acid) have attracted great attention because the hydrogen released from their aqueous solutions is fast, convenient, and controllable in the presence of a suitable catalyst.[172–174] Here, we mainly introduce the performance of zeolite-encapsulated metal catalysts in hydrogen production from ammonia borane and formic acid.

6.3.1 The hydrolysis of ammonia borane. Due to the high hydrogen storage capacities, ammonia borane (AB) has been considered as a remarkable liquid-phase hydrogen storage material and has great potential for hydrogen generation. In recent years, zeolite-encapsulated metal catalysts have showed superior hydrogen generation rates and excellent recycling stability in the hydrolysis of ammonia borane. Özkar *et al.*[147] reported the preparation of Rh nanoparticles confined in zeolite NaY *via* an ion-exchanging procedure. The HR-TEM results revealed that Rh nanoparticles (1.2 wt%) were distributed in the cages of zeolite-Y. The Rh@NaY catalyst exhibited excellent catalytic activity of the AB hydrolysis, giving a TOF value of 92 min^{-1} and unprecedented lifetime with turnovers of 47 200 over 315 h before deactivation. Recently, Yu *et al.*[77] encapsulated single Rh atoms in S-1 zeolite (Rh@S-1-H) using a direct H_2 reduction strategy under *in situ* hydrothermal conditions. Cs-corrected HAADF-STEM measurements showed that Rh atoms in Rh@S-1-H were homogeneously distributed in 5-MRs of the S-1 zeolite, while Rh metals in Rh@S-1-C (prepared by conventional calcination-reduction treatment) existed in the form of clusters. In AB hydrolysis reaction, the Rh@S-1-H catalyst exhibited excellent catalytic activity with a TOF value of 432 min^{-1}, which was two times higher than that of Rh@S-1-C (195 min^{-1}). In addition, the Rh@S-1-H catalyst possessed outstanding recycling durability, and the H_2 generation rate remained unchanged after five consecutive cycles. Following this work, Yu *et al.*[148] synthesized Rh-based bimetallic cluster

catalysts on self-pillared S-1 (SP-S-1) zeolite using the impregnation–reduction method. Benefiting from the large external surface areas and abundant Si–OH groups of self-pillared S-1 zeolite, bimetallic clusters were uniformly encaged throughout the S-1 zeolite (<1 nm). With the aid of the synergistic effect, the H_2 generation rate from AB hydrolysis was significantly improved compared to monometallic cluster catalysts, and $Rh_{0.8}Ru_{0.2}$/SP-S-1 exhibited an excellent activity with a TOF value of 620 min^{-1}, which was much higher than that of Rh/SP-S-1 (430 min^{-1}). Moreover, the catalytic activity over $Rh_{0.8}Ru_{0.2}$/SP-ZSM-5 was further improved due to the increase in zeolite acidity; the TOF value of $Rh_{0.8}Ru_{0.2}$/SP-ZSM-5 (Si/Al = 100) reached 1006 min^{-1}.

6.3.2 The dehydrogenation of formic acid. The decomposition of formic acid (FA) has two possible pathways: FA dehydrogenation to produce H_2 and CO_2 or FA dehydration to yield H_2O and CO (undesired reaction process).[175] In the presence of zeolite-encapsulated metal catalysts, the latter pathways could be avoided, and H_2 generation could be efficiently improved. For example, Deng *et al.*[149] reported the *in situ* encapsulation of subnanometer Pd nanoparticles within purely siliceous silicalite-2 (MEI structure) zeolite crystals (Pd@S-2). Based on the HAADF-STEM images, Pd nanoparticles were uniformly dispersed in S-2 zeolite crystals with an average size of 1.5 nm. The as-prepared Pd@S-2 exhibited excellent catalytic activity for the dehydrogenation of FA; 226 mL CO free gas could be released toward 100% conversion of FA within 18 min, affording a high TOF of 2009 h^{-1} and 3349 h^{-1} at 30 °C and 50 °C, respectively. The Pd@S-2 catalyst showed excellent recyclability, the H_2 generation rate decreased slightly after five consecutive cycles. In addition, the Pd@S-2 catalyst possessed superior thermal stability, the particle size of Pd nanoparticles remained basically unchanged after exposure to N_2 atmosphere at 700 °C for 2 h. Adding nonnoble-metal species to Pd-based catalysts can not only reduce the use of Pd metals but also improve the catalytic activity for the dehydrogenation of FA because of the synergistic effect of various metal components. Yu *et al.*[45] encaged bimetallic clusters Pd–$Ni(OH)_2$ in the S-1 zeolite by a hydrothermal synthesis method. Cs-corrected HAADF-STEM results revealed that the Pd and $Ni(OH)_2$ clusters were located in the intersectional spaces between the straight and sinusoidal channels of the MFI structure. EXAFS analyses showed that the average coordination number of the Pd–Pd bond in 0.8Pd–0.2$Ni(OH)_2$@S-1 was 3.1, further proving the formation of subnanometric Pd confined within the S-1 zeolite. The 0.8Pd–0.2$Ni(OH)_2$@S-1 catalyst showed outstanding catalytic activity of FA dehydrogenation, giving a TOF value of 1879 h^{-1} at 60 °C, which was nine times higher than that of Pd@S-1. DFT calculations demonstrated that the interface effect between Pd and $Ni(OH)_2$ clusters can effectively reduce the activation barrier for FA dehydrogenation and improve the catalytic performance. In addition, Mn metal was also added to Pd-based catalysts to catalyze the dehydrogenation of FA and exhibited superior catalytic activity.[150]

7 Conclusion and outlook

Metal species confined in zeolites is an important type of heterogeneous catalysts. In the past decade, zeolite-encapsulated metal catalysts have been used in many catalytic processes and exhibit excellent performance. In this review, we presented a brief summary of the most representative research progresses on zeolite-encapsulated metal catalysts. For encapsulating metal species in zeolites, two main type method, including post-treatment (*i.e.*, ion-exchanging, interzeolite transformation, and recrystallization) and *in situ* synthesis (*i.e.*, *in situ* hydrothermal and dry-gel synthesis) are introduced and compared. For the characterization of metal@zeolite, high-resolution electron microscopy techniques, XAS, CO-FTIR, XPS, and H_2-TPR have been presented to explore the unique physiochemical properties of confined metal species. For the performance of metal@zeolite, the activity, selectivity, and stability are emphasized, and the applications in important catalytic reactions such as PDH, CO and CO_2 hydrogenation, biomass conversion, and hydrogen generation are summarized.

The synthesis of metal@zeolite has been frequently reported in the last few years. However, many challenges remain to be addressed. In fact, an effective method to prepare zeolite-encapsulated single-atom metal catalysts is desired as the metal loading encapsulated within zeolite is generally too low (<2 wt%). The current synthesis strategies mostly result in metal clusters or nanoparticles encapsulated in zeolites, which is suitable for the noble metal catalyst system. Nonnoble metals are more prone to agglomerate into large particles under the synthesis and reduction process. So far, zeolite-encapsulated ultrasmall nonnoble metal catalysts, especially those with high thermal stability, are still rarely reported. Thus, effective methods to confine ultrasmall nonnoble metal clusters or single nonnoble metal atom in zeolites is significant for developing efficient nonnoble metal catalyst. The fabrication of defects or/and utilization of the strong spatial confinement effects of specific positions (*e.g.*, small pores and cavities) is a useful way to obtain stable ultrasmall nonnoble metals. Specifically, the single metal atom confined in zeolites has been realized by incorporating transitional metal species into the zeolite framework.

For clarifying the catalytic consequence of the encapsulated metal catalyst, distinguishing the location and structure of confined metals species is the way forward. Advanced characterization technologies have been used to characterize active metal sites encapsulated in zeolites. However, the locations and microenvironments of the encapsulated metal species are so complex that it is difficult to obtain accurate structural information by one means of characterization alone. Therefore, a combination of multiple characterization tools such as atomic-resolution spectroscopic and microscopic techniques seems to be an effective method to obtain structural information about the active metal sites in zeolites. In addition, the chemical states and coordination environment of metal species confined in zeolites may change in the reaction

progress. Thus, in further research, more efforts should be devoted to the development of *in situ* or operando characterization techniques.

The confinement effect of zeolites can effectively improve the catalytic performance of metal catalysts. The synergic effect between acid sites and metal sites is also important for the application of zeolite-encapsulated metal catalysts. The proximity of metal and acid sites promotes the activity of metal catalysts and change the steps of tandem reaction to gain target products. In future research, more efforts should be devoted to designing and optimizing the synergy of metal species and acid of zeolites. Through this review, we hope to help researchers understand the confinement effect of zeolites. At the same time, it provides a reference for designing zeolite-encapsulated metal catalysts with better performance.

Conflicts of interest

The authors declare no conflict of interest.

Acknowledgements

This work was supported by National Key R&D Program of China (2022YFB3805602), the CNPC Innovation Found (2021DQ02-0702).

References

1 G. Lee, W. J. Jeong and H. G. Ahn, Selective hydrogenation of acetylene to ethylene over nanosized gold and palladium supported catalysts, *J. Nanosci. Nanotechnol.*, 2020, **20**, 5800–5803.
2 S. Amdouni, Y. Cherifi, Y. Coffinier, A. Addad, M. A. Zaïbi, M. Oueslati and R. Boukherroub, Gold nanoparticles coated silicon nanowires for efficient catalytic and photocatalytic applications, *Mater. Sci. Semicond. Process.*, 2018, **75**, 206–213.
3 C. F. Lee, Y. C. Liu and S. S. Badsara, Transition-metal-catalyzed C-S bond coupling reaction, *Chem. - Asian J.*, 2014, **9**, 706–722.
4 Z. J. Li, D. H. Wang, Y. E. Wu and Y. D. Li, Recent advances in the precise control of isolated single-site catalysts by chemical methods, *Natl. Sci. Rev.*, 2018, **5**, 673–689.
5 L. C. Liu and A. Corma, Confining isolated atoms and clusters in crystalline porous materials for catalysis, *Nat. Rev. Mater.*, 2021, **6**, 244–263.
6 T. W. Hansen, A. T. DeLaRiva, S. R. Challa and A. K. Datye, Sintering of catalytic nanoparticles: particle migration or Ostwald ripening?, *Acc. Chem. Res.*, 2013, **46**, 1720–1730.
7 L. C. Liu, D. M. Meira, R. Arenal, P. Concepcion, A. V. Puga and A. Corma, Determination of the evolution of heterogeneous single metal atoms and nanoclusters under reaction conditions: Which are the working catalytic sites?, *ACS Catal.*, 2019, **9**, 10626–10639.
8 K. Wettergren, F. F. Schweinberger, D. Deiana, C. J. Ridge, A. S. Crampton, M. D. Rötzer, T. W. Hansen, V. P. Zhdanov, U. Heiz and C. Langhammer, High sintering resistance of size-selected platinum cluster catalysts by suppressed Ostwald ripening, *Nano Lett.*, 2014, **14**, 5803–5809.
9 F. Z. Song, Q. L. Zhu, N. Tsumori and Q. Xu, Diamine-alkalized reduced graphene oxide: Immobilization of sub-2 nm palladium nanoparticles and optimization of catalytic activity for dehydrogenation of formic acid, *ACS Catal.*, 2015, **5**, 5141–5144.
10 Z. L. Wang, H. L. Wang, J. M. Yan, Y. Ping, S. I. O, S. J. Lia and Q. Jiang, DNA-directed growth of ultrafine CoAuPd nanoparticles on graphene as efficient catalysts for formic acid dehydrogenation, *Chem. Commun.*, 2014, **50**, 2732–2734.
11 C. Su, S. D. Zhao, P. Wang, W. W. Chang, K. S. Chang and H. B. Zhang, Synthesis and characterization of ultrafined palladium nanoparticles decorated on 2D magnetic graphene oxide nanosheets and their application for catalytic reduction of 4-nitrophenol, *J. Environ. Chem. Eng.*, 2016, **4**, 3433–3440.
12 Q. L. Zhu, N. Tsumori and Q. Xu, Immobilizing extremely catalytically active palladium nanoparticles to carbon nanospheres: A weakly-capping growth approach, *J. Am. Chem. Soc.*, 2015, **137**, 11743–11748.
13 X. J. Gu, Z. H. Lu, H. L. Jiang, T. Akita and Q. Xu, Synergistic catalysis of metal-organic framework-immobilized Au-Pd nanoparticles in dehydrogenation of formic acid for chemical hydrogen storage, *J. Am. Chem. Soc.*, 2011, **133**, 11822–11825.
14 H. M. Dai, B. Q. Xia, L. Wen, C. Du, J. Su, W. Luo and G. Z. Cheng, Synergistic catalysis of AgPd@ZIF-8 on dehydrogenation of formic acid, *Appl. Catal., B*, 2015, **165**, 57–62.
15 H. L. Yang, Q. G. Liu, Y. Li, K. A. Sun, Z. Q. Chen, Q. Peng and C. Chen, Isolated single-atom ruthenium anchored on beta zeolite as an efficient heterogeneous catalyst for styrene epoxidation, *ChemNanoMat*, 2022, **6**, 1647–1651.
16 Y. W. Liu, Z. Li, Q. Y. Yu, Y. F. Chen, Z. W. Chai, G. F. Zhao, S. J. Liu, W. C. Cheong, Y. Pan, Q. H. Zhang, L. Gu, L. R. Zheng, Y. Wang, Y. Lu, D. S. Wang, C. Chen, Q. Peng, Y. Q. Liu, L. M. Liu, J. S. Chen and Y. D. Li, A general strategy for fabricating isolated single metal atomic site catalysts in Y zeolite, *J. Am. Chem. Soc.*, 2019, **141**, 9305–9311.
17 L. J. Xie, R. Wang, Y. C. Chai, X. F. Weng, N. J. Guan and L. D. Li, Propane dehydrogenation catalyzed by in-situ partially reduced zinc cations confined in zeolites, *J. Energy Chem.*, 2021, **63**, 262–269.
18 W. M. H. Sachtler and Z. C. Zhang, Zeolite-supported transition metal catalysts, *Adv. Catal.*, 1993, **29**, 129–220.
19 D. Farrusseng and A. Tuel, Perspectives on zeolite-encapsulated metal nanoparticles and their applications in catalysis, *New J. Chem.*, 2016, **40**, 3933–3949.
20 B. Y. Wei, X. F. Liu, Q. Y. Chang, S. G. Li, H. Luo, K. M. Hua, S. N. Zhang, J. J. Chen, Z. L. Shao, C. J. Huang, H. Wang and Y. H. Sun, Single-atom gold species within zeolite for efficient hydroformylation, *Chem Catal.*, 2022, **2**, 1–11.
21 Z. Q. Ou, Y. Z. Li, W. C. Wu, Y. F. Bi, E. H. Xing and T. W. Yu, Encapsulating subnanometric metal clusters in zeolites

for catalysis and their challenges, *Chem. Eng. J.*, 2022, **430**, 132925–132941.

22 Y. Q. Wang, C. T. Wang, L. X. Wang, L. Wang and F.-S. Xiao, Zeolite fixed metal nanoparticles: New perspective in catalysis, *Acc. Chem. Res.*, 2021, **54**, 2579–2590.

23 P. Barbaro, F. Liguori, N. Linares and C. M. Marrodan, Heterogeneous bifunctional metal/acid catalysts for selective chemical processes, *ChemInform*, 2012, **2012**, 3807–3823.

24 S. Sartipi, M. Makkee, F. Kapteijn and J. Gascon, Catalysis engineering of bifunctional solids for the one-step synthesis of liquid fuels from syngas: A review, *Catal. Sci. Technol.*, 2014, **4**, 893–907.

25 P. Mériaudeau and C. Naccache, Dehydrocyclization of alkanes over zeolite-supported metal catalysts: Monofunctional or bifunctional route, *Catal. Rev.: Sci. Eng.*, 1997, **39**, 5–48.

26 H. J. Cho, D. Y. Kim, J. Li, D. Su and B. J. Xu, Zeolite-encapsulated Pt nanoparticles for tandem catalysis, *J. Am. Chem. Soc.*, 2018, **140**, 13514–13520.

27 H. J. Cho, D. Y. Kim, S. Li, D. Su, D. Ma and B. J. Xu, Molecular-level proximity of metal and acid sites in zeolite-encapsulated Pt nanoparticles for selective multistep tandem catalysis, *ACS Catal.*, 2020, **10**, 3340–3348.

28 T. Iida, D. Zanchet, K. Ohara, T. Wakihara and Y. Román-Leshkov, Concerted bimetallic nanocluster synthesis and encapsulation via induced zeolite framework demetallation for shape and substrate selective heterogeneous catalysis, *Angew. Chem., Int. Ed.*, 2018, **57**, 6564–6568.

29 M. A. Deimund, J. Labinger and M. E. Davis, Nickel-exchanged zincosilicate catalysts for the oligomerization of propylene, *ACS Catal.*, 2014, **4**, 4189–4195.

30 A. Kurbanova, D. Zákutná, K. Gołąbek, M. Mazur and J. Přech, Preparation of Fe@MFI and CuFe@MFI composite hydrogenation catalysts by reductive demetallation of Fe-zeolites, *Catal. Today*, 2022, **390–391**, 306–315.

31 Z. Y. Zhang, Q. B. Xiao and J. Gu, Effective synthesis of zeolite-encapsulated Ni nanoparticles with excellent catalytic performance for hydrogenation of CO_2 to CH_4, *Dalton Trans.*, 2020, **49**, 14771–14775.

32 S. Wang, Z. J. Zhao, X. Chang, J. B. Zhao, H. Tian, C. S. Yang, M. R. Li, Q. Fu, R. T. Mu and J. L. Gong, Activation and spillover of hydrogen on sub-1 nm palladium nanoclusters confined within sodalite zeolite for the semi-hydrogenation of alkynes, *Angew. Chem.*, 2019, **131**, 7750–7754.

33 Z. L. Shao, S. N. Zhang, X. F. Liu, H. Luo, C. J. Huang, H. Z. Zhou, Z. X. Wu, J. Li, Hui Wang and Y. H. Sun, Maximizing the synergistic effect between Pt^0 and $Pt^{\delta+}$ in a confined Pt-based catalyst for durable hydrogen production, *Appl. Catal., B*, 2022, **316**, 121669–121680.

34 B. Li, B. Sun, X. F. Qian, W. Li, Z. X. Wu, Z. K. Sun, M. H. Qiao, M. Duke and D. Y. Zhao, In-situ crystallization route to nanorod-aggregated functional ZSM-5 microspheres, *J. Am. Chem. Soc.*, 2013, **135**, 1181–1184.

35 M. Moliner, C. Martínez and A. Corma, Synthesis strategies for preparing useful small pore zeolites and zeotypes for gas separations and catalysis, *Chem. Mater.*, 2014, **26**, 246–258.

36 Y. Ma, S. J. Song, C. C. Liu, L. M. Liu, L. K. Zhang, Y. H. Zhao, X. Wang, H. Xu, Y. J. Guan, J. G. Jiang, W. Y. Song, Y. Han, J. W. Zhang and P. Wu, Germanium-enriched double-four-membered-ring units inducing zeolite-confined subnanometric Pt clusters for efficient propane dehydrogenation, *Nat. Catal.*, 2023, **6**, 506–518.

37 Q. M. Sun, N. Wang, Q. Y. Fan, L. Zeng, A. Mayoral, S. Miao, R. O. Yang, Z. Jiang, W. Zhou, J. C. Zhang, T. J. Zhang, J. Xu, P. Zhang, J. Cheng, D. C. Yang, R. Jia, L. Li, Q. H. Zhang, Y. Wang, O. Terasaki and J. H. Yu, Subnanometer bimetallic platinum-zinc clusters in zeolites for propane dehydrogenation, *Angew. Chem., Int. Ed.*, 2020, **59**, 19450–19459.

38 R. Ryoo, J. Kim, C. Jo, S. W. Han, J. C. Kim, H. Park, J. Han, H. S. Shin and J. W. Shin, Rare-earth-platinum alloy nanoparticles in mesoporous zeolite for catalysis, *Nature*, 2020, **585**, 221–224.

39 H. G. Peng, T. Dong, S. Y. Yang, H. Chen, Z. Z. Yang, W. M. Liu, C. He, P. Wu, J. S. Tian, Y. Peng, X. F. Chu, D. S. Wu, T. C. An, Y. Wang and S. Dai, Intra-crystalline mesoporous zeolite encapsulation derived thermally robust metal nanocatalyst in deep oxidation of light alkanes, *Nat. Commun.*, 2022, **13**, 295–304.

40 P. Sazama, J. Pastvova, D. Kaucky, J. Moravkova, J. Rathousky, I. Jakubec and G. Sadovska, Does hierarchical structure affect the shape selectivity of zeolites? Example of transformation of N-hexane in hydroisomerization, *J. Catal.*, 2018, **364**, 262–270.

41 L. C. Ma, C. M. Ding, J. W. Wang, Y. F. Li, Y. N. Xue, J. Guo, K. Zhang, P. Liu and X. F. Gao, Highly dispersed Pt nanoparticles confined within hierarchical pores of silicalite-1 zeolite via crystal transformation of supported Pt/S-1 catalyst for partial oxidation of methane to syngas, *Int. J. Hydrogen Energy*, 2019, **44**, 21847–21857.

42 L. C. Liu, M. Lopez-Haro, C. W. Lopes, C. G. Li, P. Concepcion, L. Simonelli, J. J. Calvino and A. Corma, Regioselective generation and reactivity control of subnanometric platinum clusters in zeolites for high-temperature catalysis, *Nat. Mater.*, 2019, **18**, 866–873.

43 S. Molitorisová, Y. Y. Zhang, M. Kubů, A. Li, Z. Tošner and M. Shamzhy, 2D-to-3D zeolite transformation for the preparation of Pd@MWW catalysts with tuneable acidity, *Catal. Today*, 2022, **390–391**, 109–116.

44 N. Wang, Q. M. Sun, R. S. Bai, X. Li, G. Q. Guo and J. H. Yu, In situ confinement of ultrasmall Pd clusters within nanosized silicalite-1 zeolite for highly efficient catalysis of hydrogen generation, *J. Am. Chem. Soc.*, 2016, **138**, 7484–7487.

45 Q. M. Sun, N. Wang, Q. M. Bing, R. Si, J. Y. Liu, R. S. Bai, P. Zhang, M. J. Jia and J. H. Yu, Subnanometric hybrid Pd-$M(OH)_2$, M= Ni, Co, clusters in zeolites as highly efficient nanocatalysts for hydrogen generation, *Chem*, 2017, **3**, 477–493.

46 H. M. Chena, F. J. Yi, C. P. Ma, X. Gao, S. Y. Liu, Z. C. Tao, B. S. Wu, H. W. Xiang, Y. Yang and Y. W. Li,

Hydroisomerization of N-heptane on a new kind of bifunctional catalysts with palladium nanoparticles encapsulating inside zeolites, *Fuel*, 2020, **268**, 117241–117252.

47 K. H. Rasmussen, F. Goodarzi, D. B. Christensen, J. Mielby and S. Kegnæs, Stabilization of metal nanoparticle catalysts via encapsulation in mesoporous zeolites by steam-assisted recrystallization, *ACS Appl. Nano Mater.*, 2019, **2**, 8083–8091.

48 C. T. Wang, L. Wang, J. Zhang, H. Wang, J. P. Lewis and F.-S. Xiao, Product selectivity controlled by zeolite crystals in biomass hydrogenation over a palladium catalyst, *J. Am. Chem. Soc.*, 2016, **138**, 7880–7883.

49 L. Wang, G. Wang, J. Zhang, C. Bian, X. Meng and F.-S. Xiao, Controllable cyanation of carbon-hydrogen bonds by zeolite crystals over manganese oxide catalyst, *Nat. Commun.*, 2017, **8**, 15240–15247.

50 J. D. Kistler, N. Chotigkrai, P. Xu, B. Enderle, P. Praserthdam, C.-Y. Chen, N. D. Browning and B. C. Gates, A single-site platinum CO oxidation catalyst in zeolite KLTL: Microscopic and spectroscopic determination of the locations of the platinum atoms, *Angew. Chem., Int. Ed.*, 2014, **53**, 8904–8907.

51 P. Munnik, P. E. de Jongh and K. P. de Jong, Recent developments in the synthesis of supported catalysts, *Chem. Rev.*, 2015, **115**, 6687–6718.

52 J. de Graaf, A. J. van Dillen, K. P. de Jong and D. C. Koningsberger, Preparation of highly dispersed Pt particles in zeolite Y with a narrow particle size distribution: Characterization by hydrogen chemisorption, TEM, EXAFS spectroscopy, and particle modeling, *J. Catal.*, 2001, **203**, 307–321.

53 P. H. Yan, J. Mensah, A. Adesina, E. Kennedy and M. Stockenhuber, Highly-dispersed Ni on BEA catalyst prepared by ion-exchange-deposition-precipitation for improved hydrodeoxygenation activity, *Appl. Catal., B*, 2020, **267**, 118690–118699.

54 S. Song, L. Dai, G. J. Wu, W. L. Dai, N. J. Guan and L. D. Li, Meso-Zr-Al-beta zeolite as a robust catalyst for cascade reactions in biomass valorization, *Appl. Catal., B*, 2017, **205**, 393–403.

55 K. Lu, F. Jin, G. Y. Wu and Y. G. Ding, The synergetic effect of acid and nickel sites on bifunctional MWW zeolite catalysts for ethylene oligomerization and aromatization, *Sustainable Energy Fuels*, 2019, **3**, 3569–3581.

56 S. Kweon, Y. W. Kim, C. H. Shin, M. B. Park and H. K. Min, Nickel silicate beta zeolite prepared by interzeolite transformation: A highly active and stable catalyst for dry reforming of methane, *Chem. Eng. J.*, 2022, **431**, 133364–133371.

57 L. C. Liu, U. Díaz, R. Arenal, G. Agostini, P. Concepción and A. Corma, Generation of subnanometric platinum with high stability during transformation of a 2D zeolite into 3D, *Nat. Mater.*, 2017, **16**, 132–138.

58 P. Serna and B. C. Gates, Molecular metal catalysts on supports: Organometallic chemistry meets surface science, *Acc. Chem. Res.*, 2014, **47**, 2612–2620.

59 J. Zečević, A. M. J. van der Eerden, H. Friedrich, P. E. de Jongh and K. P. de Jong, Heterogeneities of the nanostructure of platinum/zeolite Y catalysts revealed by electron tomography, *ACS Nano*, 2013, **7**, 3698–3705.

60 O. Fenwick, E. Coutiño-Gonzalez, D. Grandjean, W. Baekelant, F. Richard, S. Bonacchi, D. D. Vos, P. Lievens, M. Roeffaers, J. Hofkens and P. Samorì, Tuning the energetics and tailoring the optical properties of silver clusters confined in zeolites, *Nat. Mater.*, 2016, **15**, 1017–1022.

61 K. Narsimhan, K. Iyoki, K. Dinh and Y. Román-Leshkov, Catalytic oxidation of methane into methanol over copper-exchanged zeolites with oxygen at low temperature, *ACS Cent. Sci.*, 2016, **2**, 424–429.

62 J. Y. Cai, H. Ma, J. J. Zhang, Q. Song, Z. T. Du, Y. Z. Huang and J. Xu, Gold nanoclusters confined in a supercage of Y zeolite for aerobic oxidation of HMF under mild conditions, *Chem. – Eur. J.*, 2013, **19**, 14215–14223.

63 L. H. Chen, M. H. Sun, Z. Wang, W. M. Yang, Z. K. Xie and B. L. Su, Hierarchically structured zeolites: From design to application, *Chem. Rev.*, 2020, **120**, 11194–11294.

64 Y. Zhang, C. Rao, H. G. Peng, C. Peng, L. Zhang, X. L. Xu, W. M. Liu, Z. Wang, N. Zhang and X. Wang, Enhanced toluene combustion performance over Pt loaded hierarchical porous MOR zeolite, *Chem. Eng. J.*, 2018, **334**, 10–18.

65 J. Gu, Z. Y. Zhang, P. Hu, L. P. Ding, N. H. Xue, L. M. Peng, X. F. Guo, M. Lin and W. P. Ding, Platinum nanoparticles encapsulated in MFI zeolite crystals by a two-step dry gel conversion method as a highly selective hydrogenation catalyst, *ACS Catal.*, 2015, **5**, 6893–6901.

66 M. Liu, T. Cui, X. W. Guo, J. J. Li and C. S. Song, Stable Zn@ZSM-5 catalyst via a dry gel conversion process for methanol-to-aromatics reaction, *Microporous Mesoporous Mater.*, 2021, **312**, 110696–110973.

67 Z. D. Liu, A. Chokkalingam, S. Miyagi, M. Yoshioka, T. Ishikawa, H. Yamada, K. Ohara, N. Tsunoji, Y. Naraki, T. Sano, T. Okubo and T. Wakihara, Revealing scenarios of interzeolite conversion from FAU to AEI through the variation of starting materials, *Phys. Chem. Chem. Phys.*, 2022, **24**, 4136–4146.

68 R. C. F. de Lima, D. d. S. Oliveira and S. B. C. Pergher, Interzeolitic transformation of clinoptilolite into GIS and LTA zeolite, *Minerals*, 2021, **11**, 1313–1325.

69 S. Goel, S. I. Zones and E. Iglesia, Encapsulation of metal clusters within MFI via interzeolite transformations and direct hydrothermal syntheses and catalytic consequences of their confinement, *J. Am. Chem. Soc.*, 2014, **136**, 15280–15290.

70 L. Liu, R. Arenal, D. M. Meira and A. Corma, Generation of gold nanoclusters encapsulated in an MCM-22 zeolite for the aerobic oxidation of cyclohexane, *Chem. Commun.*, 2019, **55**, 1607–1610.

71 Z. J. Wu, S. Goel, M. Choi and E. Iglesia, Hydrothermal synthesis of LTA-encapsulated metal clusters and consequences for catalyst stability, reactivity, and selectivity, *J. Catal.*, 2014, **311**, 458–468.

72 T. Otto, S. I. Zones, Y. Hong and E. Iglesia, Synthesis of highly dispersed cobalt oxide clusters encapsulated within LTA zeolites, *J. Catal.*, 2017, **356**, 173–185.
73 T. Otto, S. I. Zones and E. Iglesia, Synthetic strategies for the encapsulation of nanoparticles of Ni, Co, and Fe oxides within crystalline microporous aluminosilicates, *Microporous Mesoporous Mater.*, 2018, **270**, 10–23.
74 M. E. Davis, C. Saldarriaga and J. A. Rossin, Synthesis and catalysis of transition metal containing zeolite A, *J. Catal.*, 1987, **103**, 520–523.
75 J. A. Rossin and M. E. Davis, Synthesis of rhodium zeolite A, *J. Chem. Soc., Chem. Commun.*, 1986, 234–236.
76 S. Goel, Z. J. Wu, S. I. Zones and E. Iglesia, Synthesis and catalytic properties of metal clusters encapsulated within small-pore (SOD, GIS, ANA) zeolites, *J. Am. Chem. Soc.*, 2012, **134**, 17688–17695.
77 S. Q. M. Sun, N. Wang, T. J. Zhang, R. S. Bai, A. Mayoral, P. Zhang, Q. H. Zhang, O. Terasaki and J. H. Yu, Zeolite-encaged single-atom rhodium catalysts: Highly-efficient hydrogen generation and shape-selective tandem hydrogenation of nitroarenes, *Angew. Chem.*, 2019, **131**, 18743–18749.
78 T. Otto, S. I. Zones and E. Iglesia, Challenges and strategies in the encapsulation and stabilization of monodisperse Au clusters within zeolites, *J. Catal.*, 2016, **339**, 195–208.
79 T. Otto, X. Y. Zhou, S. I. Zones and E. Iglesia, Synthesis, characterization, and function of Au nanoparticles within TS-1 zeotypes as catalysts for alkene epoxidation using O_2/H_2O, *J. Catal.*, 2022, **410**, 206–220.
80 Y. Z. Li, Q. Q. Tan, T. T. Li, Y. Z. Tan, G. J. Yang, Y. Huang, E. H. Xing, X. W. Zhang and Q. Chen, Ultrasmall Ag clusters in situ encapsulated into silicalite-1 zeolite with controlled release behavior and enhanced antibacterial activity, *Microporous Mesoporous Mater.*, 2022, **330**, 111617–111625.
81 Z. Y. Wu, J. Zhang, Z. Su, P. Z. Wang, T. W. Tan and F.-S. Xiao, Low-temperature dehydration of ethanol to ethylene over Cu-zeolite catalysts synthesized from Cu-tetraethylenepentamine, *Ind. Eng. Chem. Res.*, 2020, **59**, 17300–17306.
82 L. Ren, L. F. Zhu, C. G. Yang, Y. M. Chen, Q. Sun, H. Y. Zhang, C. J. Li, F. Nawaz, X. J. Meng and F.-S. Xiao, Designed copper-amine complex as an efficient template for one-pot synthesis of Cu-SSZ-13 zeolite with excellent activity for selective catalytic reduction of NOx by NH_3, *Chem. Commun.*, 2011, **47**, 9789–9791.
83 S. C. Han, X. M. Tang, Y. Ma, Q. M. Wu, J. Q. Shi, J. Li, X. J. Meng, A. M. Zheng and F.-S. Xiao, Design of cobalt-amine complex as an efficient structure-directing agent for one-pot synthesis of Co-SSZ-13 zeolite, *J. Phys. Chem. C*, 2021, **125**, 16343–16349.
84 Y. C. Chai, G. J. Wu, X. Y. Liu, Y. J. Ren, W. L. Dai, C. M. Wang, Z. K. Xie, N. J. Guan and L. D. Li, Acetylene-selective hydrogenation catalyzed by cationic nickel confined in zeolite, *J. Am. Chem. Soc.*, 2019, **141**, 9920–9927.
85 T. T. Ye, H. F. Liu, F. P. Wang, H. J. Xie, S. S. Ran, W. Xu, J. Liu, B. Li, H. F. Lin, Y. M. Chai and L. Wang, Pd@silicate-1 synthesized by steam-assisted-crystallization strategy for high-efficient catalytic hydrogenation of furfural, *J. Porous Mater.*, 2022, **29**, 1479–1487.
86 J. Zhu, R. Osuga, R. Ishikawa, N. Shibata, Y. Ikuhara, J. N. Kondo, M. Ogura, J. Yu, T. Wakihara, Z. Liu and T. Okubo, Ultrafast encapsulation of metal nanoclusters into MFI zeolite in the course of its crystallization: Catalytic application for propane dehydrogenation, *Angew. Chem., Int. Ed.*, 2020, **59**, 19669–19674.
87 B. F. Zhang, G. Z. Li, S. B. Liu, Y. C. Qin, L. J. Song, L. Wang, X. W. Zhang and G. Z. Liu, Boosting propane dehydrogenation over PtZn encapsulated in an epitaxial high-crystallized zeolite with a low surface barrier, *ACS Catal.*, 2022, **12**, 1310–1314.
88 J. Q. Yang, Y. He, J. He, Y. S. Liu, H. W. Geng, S. H. Chen, L. Lin, M. Liu, T. H. Chen, Q. K. Jiang, B. M. Weckhuysen, W. H. Luo and Z. J. Wu, Enhanced catalytic performance through in situ encapsulation of ultrafine Ru clusters within a high-aluminum zeolite, *ACS Catal.*, 2022, **12**, 1847–1856.
89 J. M. Escola, D. P. Serrano, J. Aguado and L. Briones, Hydroreforming of the LDPE thermal cracking oil over hierarchical Ni/beta catalysts with different Ni particle size distributions, *Ind. Eng. Chem. Res.*, 2015, **54**, 6660–6668.
90 Y. Liu, Y. Chen, Z. Gao, X. Zhang, L. J. Zhang, M. Wang, B. B. Chen, Y. N. Diao, Y. L. Li, D. Q. Xiao, X. P. Wang, D. Ma and C. Shi, Embedding high loading and uniform Ni nanoparticles into silicalite-1 zeolite for dry reforming of methane, *Appl. Catal., B*, 2022, **307**, 121202–121210.
91 A. Villa, N. Dimitratos, C. E. Chan-Thaw, C. Hammond, G. M. Veith, D. Wang, M. Manzoli, L. Pratia and G. J. Hutchings, Characterization of gold catalysts, *Chem. Soc. Rev.*, 2016, **45**, 4953–4994.
92 Y. C. Chai, W. X. Shang, W. J. Li, G. J. Wu, W. L. Dai, N. J. Guan and L. D. Li, Nobel metal particles confined in zeolites: Synthesis, characterization, and applications, *Adv. Sci.*, 2019, **6**, 1900299–1900317.
93 M. Y. Gao, J. M. Wang, W. X. Shang, Y. C. Chai, W. L. Dai, G. J. Wu, N. J. Guan and L. D. Li, Zeolite-encaged palladium catalysts for heterogeneous Suzuki-Miyaura cross-coupling reactions, *Catal. Today*, 2023, **410**, 237–246.
94 X. Deng, B. Qin, R. Z. Liu, X. T. Qin, W. L. Dai, G. J. Wu, N. J. Guan, D. Ma and L. D. Li, Zeolite-encaged isolated platinum ions enable heterolytic dihydrogen activation and selective hydrogenations, *J. Am. Chem. Soc.*, 2021, **143**, 20898–20906.
95 R. Mishra, R. Ishikawa, A. R. Lupini and S. J. Pennycook, Single-atom dynamics in scanning transmission electron microscopy, *MRS Bull.*, 2017, **42**, 644–652.
96 D. A. T. DeLaRiva, T. W. Hansen, S. R. Challa and A. K. Datye, In situ transmission electron microscopy of catalyst sintering, *J. Catal.*, 2013, **308**, 291–305.
97 L. M. Liu, N. Wang, C. Z. Zhu, X. N. Liu, Y. H. Zhu, P. Guo, L. Alfilfil, X. L. Dong, D. L. Zhang and Y. Han, Direct imaging of atomically dispersed molybdenum that enables location of aluminum in the framework of zeolite ZSM-5, *Angew. Chem., Int. Ed.*, 2020, **59**, 819–825.

98 L. C. Liu, M. Lopez-Haro, D. M. Meira, P. Concepcion, J. J. Calvino and A. Corma, Regioselective generation of single-site iridium atoms and their evolution into stabilized subnanometric iridium clusters in MWW zeolite, *Angew. Chem., Int. Ed.*, 2020, **59**, 15695–15702.

99 J. J. Rehr, J. J. Kas, F. D. Vila, M. P. Prange and K. Jorissen, Parameter-free calculations of X-ray spectra with FEFF9, *Phys. Chem. Chem. Phys.*, 2010, **12**, 5503–5513.

100 R. Miller and J. T. Miller, An introduction to X-ray absorption spectroscopy and its in situ application to organometallic compounds and homogeneous catalysts, *Catal. Sci. Technol.*, 2012, **2**, 461–470.

101 W. J. Li, G. J. Wu, W. D. Hu, J. Dang, C. M. Wang, X. F. Weng, I. da Silva, P. Manuel, S. H. Yang, N. J. Guan and L. D. Li, Direct propylene epoxidation with molecular oxygen over cobalt-containing zeolites, *J. Am. Chem. Soc.*, 2022, **144**, 4260–4268.

102 A. Marberger, A. W. Petrov, P. Steiger, M. Elsener, O. Kröcher, M. Nachtegaal and D. Ferri, Time-resolved copper speciation during selective catalytic reduction of NO on Cu-SSZ-13, *Nat. Catal.*, 2018, **1**, 221–227.

103 Y. J. Tian, H. N. Duan, B. F. Zhang, S. Y. Gong, Z. J. Lu, L. Dai, C. Z. Qiao, G. Z. Liu and Y. Zhao, Template guiding for regioselective fabrication of uniformly sub-nanometric Pt clusters in beta-zeolites with high catalytic activity and stability, *Angew. Chem., Int. Ed.*, 2021, **60**, 21712–21717.

104 L. C. Liu and A. Corma, Identification of the active sites in supported subnanometric metal catalysts, *Nat. Catal.*, 2021, **4**, 453–456.

105 Q. Y. Song, M. H. Zhang, P. F. Li, L. Wang, X. W. Zhang and G. Z. Li, Millesimal phosphorus promoted Pd/HY for efficient hydrogenation saturation, *Mol. Catal.*, 2022, **528**, 112453–112463.

106 C. Chen, S. M. Zhang, Z. Wang and Z. Y. Yuan, Ultrasmall Co confined in the silanols of dealuminated beta zeolite: A highly active and selective catalyst for direct dehydrogenation of propane to propylene, *J. Catal.*, 2020, **383**, 77–87.

107 J. He, Z. J. Wu, Q. Q. Gu, Y. S. Liu, S. Q. Chu, S. H. Chen, Y. F. Zhang, B. Yang, T. H. Chen, A. Q. Wang, B. M. Weckhuysen, T. Zhang and W. H. Luo, Zeolite-tailored active site proximity for the efficient production of pentanoic biofuels, *Angew. Chem., Int. Ed.*, 2021, **60**, 23713–23721.

108 X. W. Lu, C. M. Guo, M. Y. Zhang, L. P. Leng, J. H. Horton, W. Wu and Z. J. Li, Rational design of palladium single-atoms and clusters supported on silicoaluminophosphate-31 by a photochemical route for chemoselective hydrodeoxygenation of vanillin, *Nano Res.*, 2021, **14**, 4347–4355.

109 P. Cao, L. Lin, H. F. Qi, R. Chen, Z. J. Wu, N. Li, T. Zhang and W. H. Luo, Zeolite-encapsulated Cu nanoparticles for the selective hydrogenation of furfural to furfuryl alcohol, *ACS Catal.*, 2021, **11**, 10246–10256.

110 H. J. Cho, D. Kim and B. J. Xu, Pore size engineering enabled selectivity control in tandem catalytic upgrading of cyclopentanone on zeolite-encapsulated Pt nanoparticles, *ACS Catal.*, 2020, **10**, 8850–8859.

111 J. J. Dai and H. B. Zhang, Recent advances in catalytic confinement effect within micro/meso-porous crystalline materials, *Small*, 2021, **17**, 2005334–2005358.

112 S. Li, L. Guo, X. He, C. Qiao and Y. Tian, Synthesis of uniform Ni nanoparticles encapsulated in ZSM-5 for selective hydrodeoxygenation of phenolics, *Renewable Energy*, 2022, **194**, 89–99.

113 H. Dai, Y. F. Shen, T. M. Yang, C. Lee, D. L. Fu, A. Agarwal, T. T. Le, M. Tsapatsis, J. C. Palmer, B. M. Weckhuysen, P. J. Dauenhauer, X. D. Zou and J. D. Rimer, Finned zeolite catalysts, *Nat. Mater.*, 2020, **19**, 1074–1080.

114 S. M. H. Sun, J. Zhou, Z. Y. Hu, L. H. Chen, L. Y. Li, Y. D. Wang, Z. K. Xie, S. Turner, G. V. Tendeloo, T. Hasan and B. L. Su, Hierarchical zeolite single-crystal reactor for excellent catalytic efficiency, *Matter*, 2020, **3**, 1226–1245.

115 S. D. Lin and M. A. Vannice, Hydrogenation of aromatic hydrocarbons over supported Pt catalysts. I. Benzene hydrogenation, *J. Catal.*, 1993, **143**, 539–572.

116 H. L. Chen, H. Yang, O. Omotoso, L. H. Ding, Y. Briker, Y. Zheng and Z. Ring, Contribution of hydrogen spillover to the hydrogenation of naphthalene over diluted Pt/RHO catalysts, *Appl. Catal., A*, 2009, **358**, 103–109.

117 J. J. Liu, H. F. Zhang, N. Y. Lu, X. L. Yan, B. B. Fan and R. F. Li, Influence of acidity of mesoporous ZSM-5-supported Pt on naphthalene hydrogenation, *Ind. Eng. Chem. Res.*, 2020, **59**, 1056–1064.

118 N. Y. Lu, J. X. Zhao, Q. Dong, Y. P. Zhao and B. B. Fan, Supported noble metal catalyst with a core-shell structure for enhancing hydrogenation performance, *Mol. Catal.*, 2021, **506**, 111543–111551.

119 C. T. Wang, E. Guan, L. Wang, X. F. Chu, Z. Y. Wu, J. Zhang, Z. Y. Yang, Y. W. Jiang, L. Zhang, X. J. Meng, B. C. Gates and F.-S. Xiao, Product selectivity controlled by nanoporous environments in zeolite crystals enveloping rhodium nanoparticle catalysts for CO_2 hydrogenation, *J. Am. Chem. Soc.*, 2019, **141**, 8482–8488.

120 J. Li, Y. L. He, L. Tan, P. P. Zhang, X. B. Peng, A. Oruganti, G. H. Yang, H. Abe, Y. Wang and N. Tsubaki, Integrated tuneable synthesis of liquid fuels via Fischer-Tropsch technology, *Nat. Catal.*, 2018, **1**, 787–793.

121 C. T. Wang, W. Fang, L. Wang and F.-S. Xiao, Fischer-Tropsch reaction within zeolite crystals for selective formation of gasoline-ranged hydrocarbons, *J. Energy Chem.*, 2021, **54**, 429–433.

122 Q. Chen, H. Z. Kang, X. Liu, K. Jiang, Y. F. Bi, Y. M. Zhou, M. Y. Wang, M. Zhang, L. Liu and E. Xing, Selective hydrogenation of aromatic ketone over Pt@Y zeolite through restricted adsorption conformation of reactants by zeolitic micropores, *ChemCatChem*, 2020, **12**, 1–6.

123 J. Zečević, G. Vanbutsele, K. P. de Jong and J. A. Martens, Nanoscale intimacy in bifunctional catalysts for selective conversion of hydrocarbons, *Nature*, 2015, **528**, 245–248.

124 J. Morávková, R. Pilař, O. Bortnovsky, D. Kaucký, A. Vondrová, J. Rathousky, G. Sádovská and P. Sazama, The

effect of the nanoscale intimacy of platinum and acid centres on the hydroisomerization of short-chain alkanes, *Appl. Catal., A*, 2022, **634**, 118535–118543.

125 G. X. Wang, S. D. Xu, L. Wang, Z. Q. Liu, X. Dong, L. X. Wang, A. M. Zheng, X. J. Meng and F.-S. Xiao, Fish-in-hole: Rationally positioning palladium into traps of zeolite crystals for sinter-resistant catalysts, *Chem. Commun.*, 2018, **54**, 3274–3277.

126 J. Zhang, L. Wang, B. S. Zhang, H. S. Zhao, U. Kolb, Y. H. Zhu, L. M. Liu, Y. Han, G. X. Wang, C. T. Wang, D. S. Su, B. C. Gates and F.-S. Xiao, Sinter-resistant metal nanoparticle catalysts achieved by immobilization within zeolite crystals via seed-directed growth, *Nat. Catal.*, 2018, **1**, 540–546.

127 D. Pakhare and J. Spivey, A review of dry (CO_2) reforming of methane over noble metal catalysts, *Chem. Soc. Rev.*, 2014, **43**, 7813–7837.

128 Z. Y. Lim, X. Q. Ma and B. M. Chen, Enhanced porosity of Ni@HSZ for dry reforming of methane, *New J. Chem.*, 2020, **44**, 1707–1710.

129 Q. L. M. Ha, H. Lund, C. Kreyenschulte, S. Bartling, H. Atia, T. H. Vuong, S. n. Wohlrab and U. Armbruster, Development of highly stable low Ni content catalyst for dry reforming of CH_4-rich feedstocks, *ChemCatChem*, 2020, **12**, 1562–1568.

130 P. Frontera, A. Aloise, A. Macario, F. Crea, P. L. Antonucci, G. Giordano and J. B. Nagy, Zeolite-supported Ni catalyst for methane reforming with carbon dioxide, *Res. Chem. Intermed.*, 2011, **37**, 267–279.

131 B. Abdullah, N. A. A. Ghani and D.-V. N. Vo, Recent advances in dry reforming of methane over Ni-based catalysts, *J. Cleaner Prod.*, 2017, **162**, 170–185.

132 C. Y. Dai, S. H. Zhang, A. F. Zhang, C. S. Song, C. Shi and X. W. Guo, Hollow zeolite encapsulated Ni-Pt bimetals for sintering and coking resistant dry reforming of methane, *J. Mater. Chem. A*, 2015, **3**, 16461–16468.

133 A. Ismaila, H. H. Chen and X. L. Fan, Nickel encapsulated in silicalite-1 zeolite catalysts for steam reforming of glycerol (SRG) towards renewable hydrogen production, *Fuel Process. Technol.*, 2022, **233**, 107306–107318.

134 M. Choi, Z. J. Wu and E. Iglesia, Mercaptosilane-assisted synthesis of metal clusters within zeolites and catalytic consequences of encapsulation, *J. Am. Chem. Soc.*, 2010, **132**, 9129–9137.

135 Q. Chen, P. Peng, G. J. Yang, Y. Z. Li, M. X. Han, Y. Z. Tan, C. X. Zhang, J. W. Chen, K. Jiang, L. Liu, C. L. Ye and E. Xing, Template guided regioselective encaging of platinum single atoms into Y zeolite: Enhanced selectivity in semihydrogenation and resistance to poisoning, *Angew. Chem., Int. Ed.*, 2022, **61**, e202205978.

136 Y. S. Wang, Z. P. Hua, X. W. Lv, L. Chen and Z. Y. Yuan, Ultrasmall PtZn bimetallic nanoclusters encapsulated in silicalite-1 zeolite with superior performance for propane dehydrogenation, *J. Catal.*, 2020, **385**, 61–69.

137 L. C. Liu, M. Lopez-Haro, C. W. Lopes, S. Rojas-Buzo, P. Concepcion, R. Manzorro, L. Simonelli, A. Sattler, P. Serna, J. J. Calvino and A. Corma, Structural modulation and direct measurement of subnanometric bimetallic PtSn clusters confined in zeolites, *Nat. Catal.*, 2020, **3**, 628–638.

138 X. T. Zhang, N. He, C. Y. Liu and H. C. Guo, Pt-Cu Alloy nanoparticles encapsulated in silicalite-1 molecular sieve: Coke-resistant catalyst for alkane dehydrogenation, *Catal. Lett.*, 2019, **149**, 974–984.

139 Y. Wang, Y. Suo, X. Lv, Z. Wang and Z. Y. Yuan, Enhanced performances of bimetallic Ga-Pt nanoclusters confined within silicalite-1 zeolite in propane dehydrogenation, *J. Colloid Interface Sci.*, 2021, **593**, 304–314.

140 M. Javed, S. L. Cheng, G. H. Zhang, C. C. Amoo, J. Y. Wang, P. Lu, C. X. Lu, C. Xing, J. Sun and N. Tsubaki, A facile solvent-free synthesis strategy for co-imbedded zeolite-based Fischer-Tropsch catalysts for direct gasoline production, *Chin. J. Catal.*, 2020, **41**, 604–612.

141 C. T. Wang, J. Zhang, J. Q. Qin, L. Wang, E. Zuidema, Q. Yang, S. S. Dang, C. Q. Yang, J. P. Xiao, X. J. Meng, C. Mesters and F.-S. Xiao, Direct conversion of syngas to ethanol within zeolite crystals, *Chem*, 2020, **6**, 646–657.

142 C. C. Amoo, M. Li, A. Noreen, Y. J. Fu, E. Maturura, C. Du, R. Q. Yang, X. H. Gao, C. Xing and N. Tsubaki, Fabricating Fe nanoparticles embedded in zeolite Y microcrystals as active catalysts for Fischer-Tropsch synthesis, *ACS Appl. Nano Mater.*, 2020, **3**, 8096–8103.

143 F. Y. Zhang, W. Zhou, X. W. Xiong, Y. H. Wang, K. Cheng, J. C. Kang, Q. H. Zhang and Y. Wang, Selective hydrogenation of CO_2 to ethanol over sodium-modified rhodium nanoparticles embedded in zeolite silicalite-1, *J. Phys. Chem. C*, 2021, **125**, 24429–24439.

144 J. W. Liu, S. M. Wu, L. Y. Wang, G. Tian, Y. Qin, J. X. Wu, X. F. Zhao, Y. X. Zhang, G. G. Chang, L. Wu, Y. X. Zhang, Z. F. Li, C. Y. Guo, C. Janiak, S. Lenaerts and X. Y. Yang, Pd/Lewis acid synergy in macroporous Pd@Na-ZSM-5 for enhancing selective conversion of biomass, *ChemCatChem*, 2020, **12**, 5364–5368.

145 Q. Chen, T. H. Li, Y. M. Zhou, Y. F. Bi, S. Guo, X. Liu, H. Z. Kang, M. Y. Wang, L. Liu, E. H. Xing and D. Y. Yang, Selective hydrogenation of 5-hydroxymethylfurfural via zeolite encapsulation to avoid further hydrodehydroxylation, *Ind. Eng. Chem. Res.*, 2020, **59**, 12004–12012.

146 W. X. Zhuang, X. L. Liu, L. Chen, P. W. Liu, H. M. Wen, Y. Zhou and J. Wang, One-pot hydrothermal synthesis of ultrafine Pd clusters within beta zeolite for selective oxidation of alcohols, *Green Chem.*, 2020, **22**, 4199–4209.

147 M. Zahmakıran and S. Özkar, Zeolite framework stabilized rhodium (0) nanoclusters catalyst for the hydrolysis of ammonia-borane in air: Outstanding catalytic activity, reusability and lifetime, *Appl. Catal., B*, 2009, **89**, 104–110.

148 N. Wang, Q. M. Sun, T. J. Zhang, A. Mayoral, L. Li, X. Zhou, J. Xu, P. Zhang and J. H. Yu, Impregnating subnanometer metallic nanocatalysts into self-pillared zeolite nanosheets, *J. Am. Chem. Soc.*, 2021, **143**, 6905–6914.

149 M. Deng, J. Ma, Y. T. Liu, Y. K. Pang, C. L. Yang, T. T. Cao, Z. H. Yuan, M. Q. Yao, F. Liu and X. D. Wang, Pd

nanoparticles confined in pure silicalite-2 zeolite with enhanced catalytic performance for the dehydrogenation of formic acid at room temperature, *Fuel*, 2023, **333**, 126466–126475.

150 Q. M. Sun, B. W. J. Chen, N. Wang, Q. He, A. Chang, C.-M. Yang, H. Asakura, T. Tanaka, M. J. Hülsey, C.-H. Wang, J. H. Yu and N. Yan, Zeolite-encaged Pd-Mn nanocatalysts for CO_2 hydrogenation and formic acid dehydrogenation, *Angew. Chem., Int. Ed.*, 2020, **59**, 20183–20191.

151 X. X. Zhu, X. P. Wang and Y. P. Su, Propane dehydrogenation over PtZn localized at Ti sites on TS-1 zeolite, *Catal. Sci. Technol.*, 2021, **11**, 4482–4490.

152 L. J. Xie, Y. C. Chai, L. L. Sun, W. L. Dai, G. J. Wu, N. J. Guan and L. D. Li, Optimizing zeolite stabilized Pt-Zn catalysts for propane dehydrogenation, *J. Energy Chem.*, 2021, **57**, 92–98.

153 W. Cai, R. T. Mu, S. J. Zha, G. D. Sun, S. Chen, Z.-J. Zhao, H. Li, H. Tian, Y. Tang, F. Tao, L. Zeng and J. L. Gong, Subsurface catalysis-mediated selectivity of dehydrogenation reaction, *Sci. Adv.*, 2018, **4**, 2375–2382.

154 K. Cheng, J. Kang, D. L. King, V. Subramanian, C. Zhou, Q. Zhang and Y. Wang, Advances in catalysis for syngas conversion to hydrocarbons, *Adv. Catal.*, 2017, **60**, 125–208.

155 Y. M. Ni, Y. Liu, Z. Y. Chen, M. Yang, H. C. Liu, Y. L. He, Y. Fu, W. L. Zhu and Z. M. Liu, Realizing and recognizing syngas-to-olefins reaction via a dual-bed catalyst, *ACS Catal.*, 2019, **9**, 1026–1032.

156 G. H. Zhang, C. C. Amoo, M. Q. Li, J. Y. Wang, C. X. Lu, P. Lu, C. Xing, X. H. Gao, R. Q. Yang and N. Tsubaki, Rational design of syngas to isoparaffins reaction route over additive dehydrogenation catalyst in a triple-bed system, *Catal. Commun.*, 2019, **131**, 105799–105803.

157 C. Du, P. Lu and N. Tsubaki, Efficient and new production methods of chemicals and liquid fuels by carbon monoxide hydrogenation, *ACS Omega*, 2020, **5**, 49–56.

158 A. Kätelhön, R. Meys, S. Deutz, S. Suh and A. Bardow, Climate change mitigation potential of carbon capture and utilization in the chemical industry, *Proc. Natl. Acad. Sci. U. S. A.*, 2019, **166**, 11187–11194.

159 Y. M. Chen, B. C. Qiu, Y. Liu and Y. Zhang, An active and stable nickel-based catalyst with embedment structure for CO_2 methanation, *Appl. Catal., B*, 2020, **269**, 118801–118809.

160 D. Wang, Z. H. Xie, M. D. Porosoff and J. G. Chen, Recent advances in carbon dioxide hydrogenation to produce olefins and aromatics, *Chem*, 2021, **7**, 2277–2311.

161 I. Nezam, W. Zhou, G. S. Gusmão, M. J. Realff, Y. Wang, A. J. Medford and C. W. Jones, Direct aromatization of CO_2 via combined CO_2 hydrogenation and zeolite-based acid catalysis, *J. CO2 Util.*, 2021, **45**, 101405–101425.

162 Q. Zhang, J. H. Yu and A. Corma, Applications of zeolites to C1 chemistry: Recent Advances, challenges, and opportunities, *Adv. Mater.*, 2020, **32**, 2002927–2002957.

163 J. Přech, D. R. Strossi Pedrolo, N. R. Marcilio, B. Gu, A. S. Peregudova, M. Mazur, V. V. Ordomsky, V. Valtchev and A. Y. Khodakov, Core-shell metal zeolite composite catalysts for in situ processing of Fischer-Tropsch hydrocarbons to gasoline type fuels, *ACS Catal.*, 2020, **10**, 2544–2555.

164 T. Li, A. Beck, F. Krumeich, L. Artiglia, M. K. Ghosalya, M. Roger, D. Ferri, O. Kröcher, V. Sushkevich, O. V. Safonova and J. A. van Bokhoven, Stable palladium oxide clusters encapsulated in silicalite-1 for complete methane oxidation, *ACS Catal.*, 2021, **11**, 7371–7382.

165 M. Moliner, J. E. Gabay, C. E. Kliewer, R. T. Carr, J. Guzman, G. L. Casty, P. Serna and A. Corma, Reversible transformation of Pt nanoparticles into single atoms inside high-silica chabazite zeolite, *J. Am. Chem. Soc.*, 2016, **138**, 15743–15750.

166 S. Wang, Z.-J. Zhao, X. Chang, J. Zhao, H. Tian, C. Yang, M. Li, Q. Fu, R. Mu and J. Gong, Activation and spillover of hydrogen on sub-1nm palladium nanoclusters confined within sodalite zeolite for the semi-hydrogenation of alkynes, *Angew. Chem., Int. Ed.*, 2019, **58**, 7668–7672.

167 W. J. Li, G. J. Wu, W. D. Hu, J. Dang, C. M. Wang, X. F. Weng, I. da Silva, P. Manuel, S. H. Yang, N. J. Guan and L. D. Li, Direct propylene epoxidation with molecular oxygen over cobalt containing zeolites, *J. Am. Chem. Soc.*, 2022, **144**, 4260–4268.

168 T. He, Y. X. Wang, P. J. Miao, J. Q. Li, J. H. Wu and Y. M. Fang, Hydrogenation of naphthalene over noble metal supported on mesoporous zeolite in the absence and presence of sulfur, *Fuel*, 2013, **106**, 365–371.

169 H. T. Wang, Q. Wang, Y. S. Wu, J. B. Peng, X.-K. Gu and M. Y. Ding, Controlling reaction pathways via selective C-O activation for highly efficient biomass oriented-upgrading, *Chem. Eng. J.*, 2022, **446**, 137404–137411.

170 J. M. Lan, P. W. Liu, P. Fu, X. L. Liu, M. L. Xie, S. Jiang, H. M. Wen, Y. Zhou and J. Wang, Palladium confined in pure-silica TON zeolite for furfuryl alcohol hydrogenation into tetrahydrofurfuryl alcohol, *Microporous Mesoporous Mater.*, 2021, **322**, 111161–111169.

171 P. He, Q. S. Yi, H. W. Geng, Y. C. Shao, M. Liu, Z. J. Wu, W. H. Luo, Y. S. Liu and V. Valtchev, Boosting the catalytic activity and stability of Ru metal clusters in hydrodeoxygenation of guaiacol through MWW zeolite pore constraints, *ACS Catal.*, 2022, **12**, 14717–14726.

172 C. L. Wang and D. Astruc, Recent developments of nanocatalyzed liquid-phase hydrogen generation, *Chem. Soc. Rev.*, 2021, **50**, 3437–3484.

173 J. Eppinger and K. W. Huang, Formic acid as a hydrogen energy carrier, *ACS Energy Lett.*, 2017, **2**, 188–195.

174 F. Valentini, V. Kozell, C. Petrucci, A. Marrocchi, Y. L. Gu, D. Gelman and L. Vaccaro, Formic acid, a biomass-derived source of energy and hydrogen for biomass upgrading, *Energy Environ. Sci.*, 2019, **12**, 2646–2664.

175 I. Barlocco, S. Capelli, X. Lu, S. Bellomi, X. Huang, D. Wang, L. Prati, N. Dimitratos, A. Roldan and A. Villa, Disclosing the role of gold on palladium-gold alloyed supported catalysts in formic acid decomposition, *ChemCatChem*, 2021, **13**, 4210–4222.